EXPERIMENTAL TECHNIQUES FOR ASTROPARTICLE PHYSICS*

Domenico Della Volpe

Université de Genève, Genève, Switzerland

(Received January 2, 2020)

The gamma-ray astronomy will reach its acme with the next generation instruments: the Cherenkov Telescope Array (CTA) and the Large High-Altitude Array Shower Observatory (LHAASO). CTA is an array of Imaging Air Cherenkov Telescopes (IACT), which detect the Cherenkov light produced by the charged particles present in the shower produced by cosmic rays when impinging on the atmosphere. LHAASO can also detect the Cherenkov and fluorescence light produced by the shower, but mostly aims at detecting directly the charged particles in the shower. Though quite different and complementary, their characteristics are deeply tied to the physics of the air shower, whose knowledge is then fundamental for understanding their design. In this paper, I will go first through the interaction between radiation and matter needed for the next step of discussing the physics of air showers. Once the physics base is set, I will go through some detection technique, illustrate the IACT approach and the EAS array, and compare them.

DOI:10.5506/APhysPolB.50.2081

1. Introduction

After more than hundred years since the discovery of the cosmic rays (CRs), their origins and production mechanism have not been established yet. The CRs are locally detected non-thermal relativistic particles but they can also be regarded as a further "substance" of the Universe after matter, radiation and magnetic field, thus pointing to more fundamental issues concerning the Universe. Over the years, many experiments have studied CRs characteristics. In Fig. 1 (left), there is shown the so-called "all-particle" CRs energy spectrum [1], which represents the flux of CRs measured at Earth that can be described as a function of the energy, by a power law with a rather sharp drop extending over several orders of magnitude. The slope of

* Presented at the LIX Cracow School of Theoretical Physics "Probing the Violent Universe with Multimessenger Eyes: Gravitational Waves, High-energy Neutrinos, Gamma Rays, and Cosmic Rays", Zakopane, Poland, June 14–22, 2019.

the spectrum seems fairly constant over a wide range suggesting that there is a universal gear mechanism and follows the relation $\mathrm{d}N/\mathrm{d}E \sim E^{-\gamma}$ with a value of $\gamma = 2.7$, called spectral index. The lowest energy particles with $E \sim 1$ GeV come mostly from the heliosphere and dominate the galactic spectrum, which is, therefore, hard to measure at these energies. The spectrum also exhibits two peculiar features, the so-called *knee* around 3×10^{15} eV and the *ankle* at about 10^{19} eV. The *knee* consists of a steepening of the spectrum to E^{-3} for energy of few PeV, and it is a crucial feature in the sense that it is where the transition from galactic to extra-galactic CRs is supposed to happen and whose slope depends on the particles charge Z. This steepening is brought back to a reduced efficiency of the galactic CRs sources in accelerating particles up to such energies, or to the reduced ability of the Galactic Magnetic Field (GMF) to confine particles above the *knee*. As a matter of fact, in many models, there is an assumption that particles have to be confined for a finite time inside the accelerator site in order to be accelerated. Therefore, the size of the site cannot be greater than the Larmor radius of the particles. Using this simple criterion, Hillas made a classification of the possible accelerators of CRs according to their size and magnetic fields as shown in Fig. 1 (right).

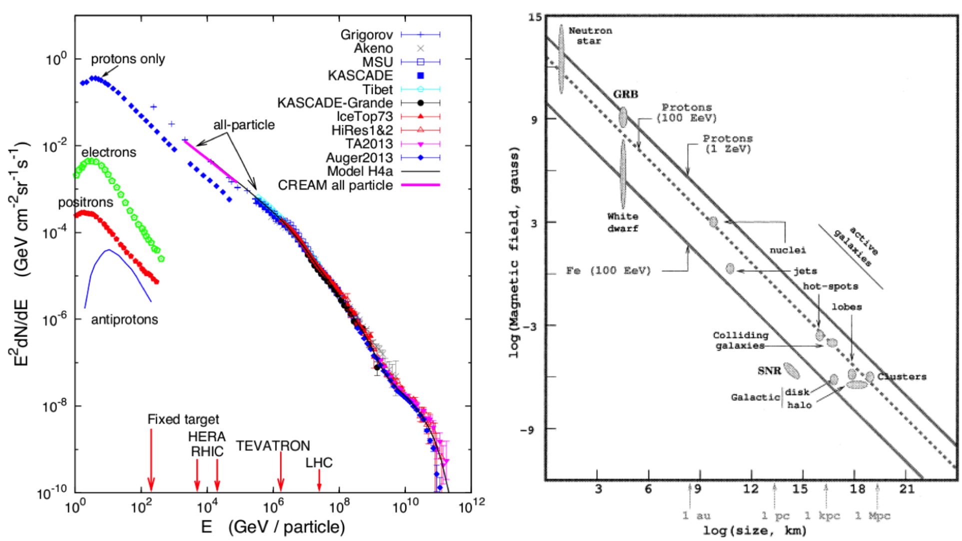

Fig. 1. Left: The all-particle spectrum of cosmic rays at Earth [2] together with the proton spectrum, as measured by different experiments. The subdominant contributions from electrons, positrons and antiprotons are measured by the PAMELA experiment. Right: A revised version [3] of the "Hillas Plot" [4], showing the magnetic field *versus* the size of potential UHECR sources.

The origin of the *knee* is believed to be related to the maximum energy attainable by particles and therefore to acceleration mechanism. In diffusive shock acceleration (DSA) model, the CRs are accelerated in blast waves of SuperNova Remnants (SNR) until they reach a limit, which depends on the particle charge Ze and the rigidity $R = pc/(Ze)$, where the DSA becomes inefficient. The maximum energy reachable by a nucleus of charge Z may range from $Z \times 10^{14}$ eV to $Z \times 10^{15}$ eV depending on the model and types of supernovae considered [5]. Light nuclei, mostly protons and hydrogen, are supposed to be the dominant component below the *knee* because heavier elements are less abundant in the inter-stellar medium (ISM). However, the contribution of heavier elements is expected to significantly increase above the *knee* given that the shocks accelerate particles according to their rigidity, and then they can reach much higher energies than hydrogen or protons. The sum of the contributions from all nuclear species to the CRs spectrum reproduces well the E^{-3} steepening above the *knee*. In this scenario, the *knee* would result from the convolution of the various cut-offs while the spectral composition would become heavier. Unfortunately, this scenario requires magnetic fields much stronger than the inter-stellar one [6] and this brings into play some sort of magnetic amplification and no convincing models exist so far. Alternative explanations can be provided by models that relate the *knee* to leakage of cosmic rays from the Galaxy. In this case, the *knee* is expected to occur at lower energies for light nuclei as compared to heavy ones due to the rigidity dependence of the Larmor radius of cosmic rays propagating in the Galactic Magnetic Field [7].

Another feature of the spectrum in Fig. 1 (left) is the *ankle*, *i.e.* the hardening of the CRs spectrum observed for particle energies around 3×10^{18} eV. It is believed to represent the energy range where the extra-galactic components of CRs take over the galactic one. The problem stays in the fact that, as said before, the *knee* represents the maximum energy at which protons can be accelerated by a galactic accelerator. Even considering the heaviest element like iron, which undergos higher accelerations given the rigidity dependence of DSA acceleration, the maximum energy reachable is still too low to reach the *ankle*. A possible scenario is that the transition happens much earlier than the *ankle*, at an energy of about 10^{17}, where another (less pronounced) feature, called the *second knee* is observed in the spectrum [8]. However, this scenario would require an unnatural amount of fine tuning to have the extra-galactic contribution appearing sharply exactly where the galactic one disappears, in contrast to the simple case of the hardening of the spectrum where such a fine tuning is not required. In addition, another explanation for the *ankle* would be needed. An alternative scenario is that there exists a third CRs population that would fill the gap between the SNR component and the extra-galactic one [6], or that a subset of the SNR population, rather than a new source class, fills the gap [9]. For a full review, please see Ref. [10]. The Ultra-High Energy (UHE) CRs, with energies ranging from the *ankle* to 100 EeV, have a flatter slope that ends at the "GZK" cut-off [11, 12] caused by photo-pion production on the Cosmic Microwave Background (CMB). At that energies, the CRs can interact with the CMB photons producing the resonance Δ^+ via the process $p+\gamma_{\mathrm{CMB}} \rightarrow \Delta^+$, which decays in pions of lower energy. This process then limits to about 50 Mpc — the maximum distance CRs can travel from their source.

Though this spectrum is a consolidated experimental reality, its shape and features, as where the transition between galactic and extra-galactic sources happens or which exactly are the sources contributing to the flux, have not been established yet. Theories for acceleration mechanisms in the sources and for propagation of cosmic rays exist, but yet none can explain all the features of the spectrum and the cosmic-ray composition as a function of energy. Moreover, the particles propagate diffusively in the Interstellar Medium (ISM) over very long distances and under the effect of the Galactic Magnetic Fields (GMF) and the spectrum is folding of three mechanisms: the acceleration inside the sources, the escape from the sources and the propagation across the Galaxy. Understanding the origin of CRs and their propagation through ISM is then a fundamental quest in the understanding of the structure and nature of the Universe (see [2] and references therein). In particular, the identification of galactic sources able to accelerate particles up to PeV energies, the so-called "PeVatrons", is still missing. Nonetheless, no major question on cosmic rays, their production and propagation characteristics, or their origin could not be answered. It is evident that only accumulating a sufficient statistic of astrophysical objects can allow detailed studies of their characteristics and shed some light on these long-standing quests. This requires improving the instruments' sensitivity, energy range covered and also effective area. In this scenario, the next generation experiments for gamma-ray astronomy and cosmic-rays' studies are born: the Cherenkov Telescope Array (CTA) and the Large High-Altitude Array Shower Observatory (LHAASO). CTA is an array of almost hundred Imaging Air Cherenkov Telescopes (IACT), distributed in two sites, a northern site in the Canary Island and the southern site in the desert of Paranal in Chile. Its construction will start in coming years and it will not finish before 2025. LHAASO is an Extended Air-Shower (EAS) array, under construction in the Sichuan region of the China, which should be completed by the end of 2020. LHAASO is composed of different elements and type of detectors covering an area of more than a square kilometre.

Despite the different technique used to detect shower and the different technologies used, they all aim at measuring for each shower, the energy, the direction and identify the type of primary particle which started it. How this is done, and which are the advantages and limitations of these two complementary approaches, needs a good understanding of the underlying physics of the showers.

2. The physics of air showers

2.1. Interaction of radiation a matter

The starting point for a correct understanding of the physics of air showers is to discuss briefly the phenomena associated with the radiation interaction in matter. Charged particles, heavier than electrons, lose energy while traversing matter mainly through the excitation and ionisation of atoms of the medium. For heavy ions, with velocity of the order (or lower) of the Bohr orbital velocity of electrons in the hydrogen atom, the energy loss due to collisions with target nuclei is no longer negligible. Electrons (and positrons) being much lighter can transfer higher energies to the electrons of the atoms and reach at not-too-high energies the so-called critical energy, where they start to lose energy by radiating photons. Neutral particles are, in general, detected through particles that are produced in their interaction with matter, either charged as light mesons, muons or electrons or photons as in the $\pi^0 \to \gamma\gamma$ process. The most relevant processes for photon absorption in matter are the photo-electric effect, the Compton scattering and pair-production. Here, it is given just a brief remainder of relevant concepts. For a more extensive and coherent treatment of this topic, please refer to the PDG review[1] and references therein or to major text books [13–19]. Let us start by discussing the interaction between charged particles and matter. In Fig. 2, there are schematically shown some of the most relevant processes arising when a particle impinges on matter.

The particle can be regarded as a "probe" of matter as it will "resolve" the matter structure depending on its energy. The type of process is mostly depending on the particle wavelength $\lambda = \hbar/p$, *i.e.* its energy. As shown in Fig. 2, for wavelength below the angstrom (12.5 keV), the particle "sees" matter as continuous medium. In this case, the particle field polarises the medium and can give rise to phenomena like the Cherenkov emission or the transition radiation emission. Around 10 keV, the particle starts to "see" the atomic structure of matter and interacts mostly with the electrons of the outer shells. At energies greater than few GeV, corresponding to a wavelength of the order of the atomic nucleus (fm), it can interact with electron from the inner shells or directly with the nuclei.

A fundamental quantity, used in describing interactions, is the cross section. The concept, though quite simple and intuitive, is, in truth, a very powerful tool to investigate a plethora of phenomena. Let us consider an ideal experiment in which a flux of monochromatic particles ϕ impinges on a slab of material and it is deflected through elastic collision[2]. A flux of particles can be well-approximated by a beam of particles, uniformly

---

[1] PDG review — passage of particles through matter (`http://pdg.lbl.gov/2019/reviews/rpp2018-rev-passage-particles-matter.pdf`).

[2] The cross section can be applied to a much wider range of interactions, but here we go to the simplest approximation, as the scope is purely illustrative.

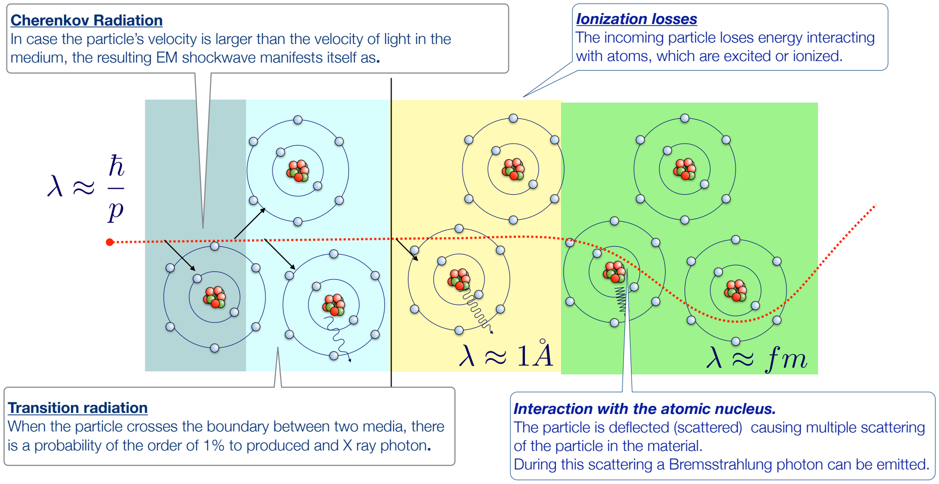

Fig. 2. Interaction of charged particle with matter. The phenomena involved, as shown in the picture, depend on energy, *i.e.* then de Broglie wavelength of the particle.

distributed in space and time, whose size is much larger than the target size. If we do a simple counting experiment in which we measure the number of particles emerging after the interaction scattered into the solid angle $\mathrm{d}\Omega$ per unit time, we can say that the probability of interaction of the single projectile particles with a nucleus of the target is

$$\frac{\mathrm{d}\sigma}{\mathrm{d}\Omega} = \frac{1}{\phi}\frac{\mathrm{d}N_{\mathrm{s}}}{\mathrm{d}\Omega}\,. \tag{1}$$

The quantity N_{s} is the average number of particles scattered per unit time. In fact, the number of particles scattered fluctuates over different finite time of measurements, because of the randomness of the impact parameter. At the same time, averaging over many finite time windows this number tends to a fixed value N_{s}. The quantity in Eq. (1) represents the probability of interaction of a single particle in the beam with a single atom in the target. It then gives information on the structure of the interaction and on the potential governing it. It is astonishing how a simple counting experiment is able to probe a so fundamental quantity as the interaction structure!

The cross section has the dimension of an area, given the definition of the flux ϕ, and it is then measured in cm^2. Therefore, a naive interpretation of σ is the geometrical crossing area between the target and the beam. This also explains the unit used to measure the cross section, the barn

$$1\,\mathrm{b} = 10^{-24}\ \mathrm{cm}^2 = 10^{-28}\ \mathrm{m}^2 = 100\ \mathrm{fm}^2\,.$$

The barn corresponds approximately to the cross-sectional area of the uranium atoms and the word was created at time of the Manhattan projects as a secret word to refer to the cross section [20]. Starting from the cross section we can define another important quantity which is the *mean free path*, *i.e.* the average distance between two successive interactions. If N represents the linear density of target, then by definition, the probability to undergo an interaction after 1 interaction length is equal to one. Thus,

$$N\sigma\lambda = 1 \qquad \Longrightarrow \qquad \lambda = \frac{1}{N\sigma}\,. \tag{2}$$

This heuristic derivation of λ can be obtained more rigorously using probability. With this definition, the survival probability P_{s} and the interaction probability P_{int} are

$$P_{\mathrm{s}}(x) = \mathrm{e}^{-N\sigma x} = \mathrm{e}^{-\frac{x}{\lambda}}\,, \qquad P_{\mathrm{int}} = 1 - \mathrm{e}^{-\frac{x}{\lambda}}\,. \tag{3}$$

The mean free path is a quantity widely used in many physics fields, but in particle physics it is mostly referred to as the interaction length for hadron nuclear interaction, or absorption length for photons. As a matter of fact, in both cases, it represents the length after which the initial flux is reduced by 1/e due to the interaction.

2.1.1. Interaction of charged particles

When a charged particle of mass m greater than the electron mass m_e [3] traverse, a slab of material $\mathrm{d}x$ have a finite probability to lose a fraction $\mathrm{d}E$ of its energy interacting with the electrons of the outer shells.

This energy loss is governed by the Bethe–Bloch [21, 22] formula reported below as

$$-\frac{\mathrm{d}E}{\mathrm{d}x} = 4\pi N_A r_e^2 m_e c^2 z^2 \frac{Z}{A}\frac{1}{\beta^2}\left[\frac{1}{2}\ln\left(\frac{2m_e c^2\gamma^2\beta^2 W_{\mathrm{max}}}{I}\right) - \beta^2 - \frac{\delta(\beta\gamma)}{2} - \frac{C}{Z}\right]. \tag{4}$$

The quantity W_{max} is the maximum energy transferred in an elastic collision between a particle of mass M and the atom's electrons

$$W_{\mathrm{max}} = \frac{2m_e c^2\beta^2\gamma^2}{1 + 2\gamma m_e/M + (m_e/M)^2}\,, \tag{5}$$

which for $M \gg m_e$ reduces to $W_{\mathrm{max}} \approx 2m_e c^2\beta^2\gamma^2$. The formula was originally calculated under the classical approximation, considering only the electromagnetic interaction between the Z electrons of the target nucleus

[3] The case of the electron as an impinging particle has to be treated differently as we will show later in Sec. 2.1.2.

and the particle with charge Ze. It is interesting to note that, as shown in Fig. 3, there are different regimes for the energy loss as a function of the quantity $\beta\gamma = p/Mc$, which is independent of the particle mass, giving an universal description of the energy loss features.

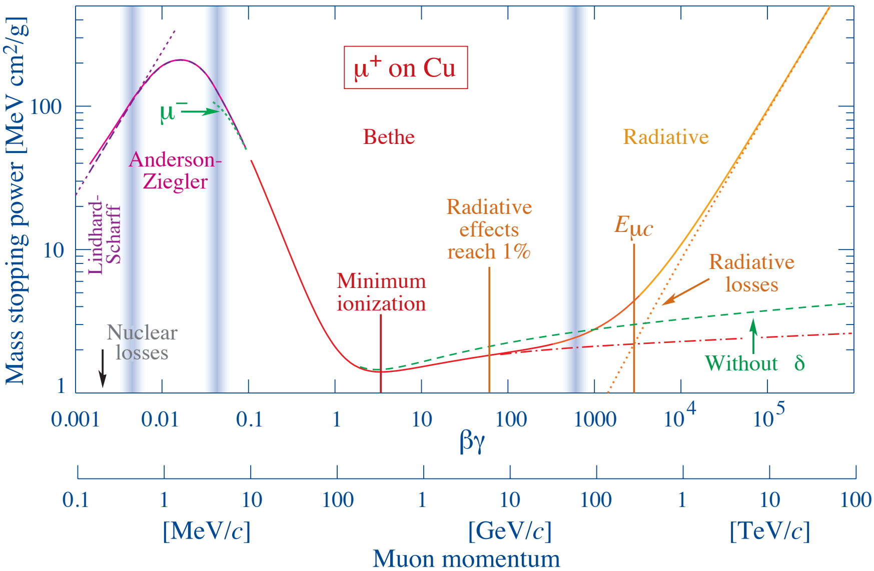

Fig. 3. The energy loss for a positive muon transversing copper as a function of $\beta\gamma$ over nine orders of magnitude in momentum (12 orders of magnitude in kinetic energy) [23].

For $\beta\gamma < 1$, the particles energy loss is proportional to $1/\beta^2$. In this regime, the particle energy losses are relevant and contribute to the stopping of the particle. As a matter of fact, at each interaction, the β is reduced and the energy lost increases further causing the particle to lose its energy until it stops. This can be heuristically understood as due to the fact that a slow particle feels the electric field of atom's electrons for a longer time. It is also important to note the dependence on Z^2 of the primary particle as it implies that heavier nuclei experience larger energy loss and then the shower development and size are different depending on Z. This is known since the first balloon experiments with emulsions and was shown in a famous picture by Powell, Fowler and Perkins in their book [24], where it was shown how the thickness of the track for different nuclei was increasing with Z.

For $\beta\gamma \approx 3.5$, the energy loss reaches a minimum. Most relativistic particles (*e.g.*, cosmic-ray muons) have mean energy loss rates close to the minimum, and they are, therefore, called minimum-ionizing particles or MIPs. As the particle energy increases, its electric field flattens and extends, due to the relativistic regime, so that the distant-collision contribution to energy losses increases logarithmically with $\beta\gamma$. However, real media become polarised, limiting the field extension and effectively truncating this part of the logarithmic rise. This is taken into account by the density correction effect, represented by δ in Eq. (4) and also shown in Fig. 3. At much higher energies, for $\beta > 1000$, the particles can undergo radiative losses, as bremsstrahlung becomes more and more dominant.

The energy at which the radiative losses take over the ionisation is called the critical energy E_{C} and plays a fundamental role in the shower development. It represents, in fact, the energy at which the shower stops to develop, and the shower particles start to be absorbed as they do not have enough energy to produce new child particles. It is also important to note the linear dependence of the energy loss with the material (Z), shown in Fig. 4 (left). Even if it has a linear behaviour, the energy loss is within 1 MeV for Z ranging from 1 to 100 so, in general, at first order can be safely assumed to be around 1.5 $\mathrm{MeV/g\,cm^{-2}}$. For gas and, in general, for the atmosphere, the energy is around 2.2 $\mathrm{MeV/g\,cm^{-2}}$. This is a good approximation for all materials but the liquid hydrogen which has a factor two greater energy loss (see Fig. 4 (right)).

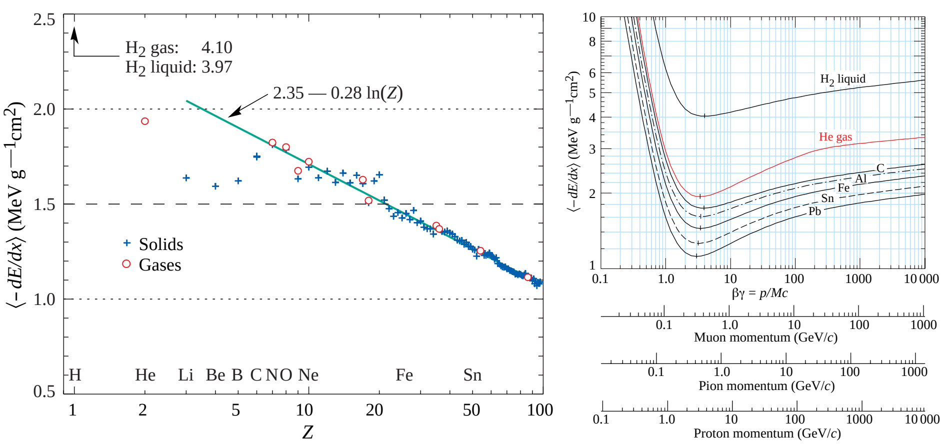

Fig. 4. Energy loss as a function of Z (left) and the $\mathrm{d}E/\mathrm{d}x$ as a function of $\beta\gamma$ for different materials [23].

2.1.2. Interactions of electrons with matter

At low energies, electrons and positrons lose energy primarily via ionisation although other processes contribute, as shown in Fig. 5. In the case of the electron/positrons, the Bethe–Block needs to be modified to take into account the fact that the mass of the impinging particle is the same as of the atom's electrons, and also the different charge between electron and positrons is important.

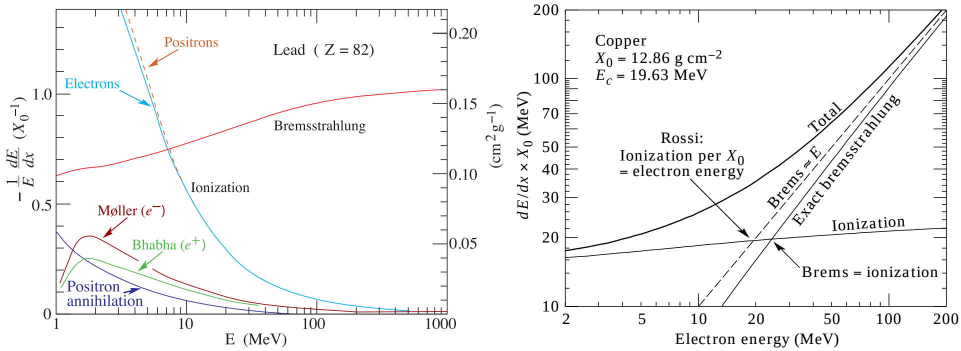

Fig. 5. Left: Fractional energy loss per radiation length in lead as a function of electron or positron energy. Right: Two different definition of critical energy E_C marked by the arrows [23].

In the case of the electron, the particle mass is $M = m_e$ and then Eq. (4) needs to be modified to take into account the different kinematics. In truth, more relevant is the fact that in this case, there is an interaction between indistinguishable particles and the quantum effect becomes more important. In addition, the situation is slightly different for electrons and positrons. The Bethe–Block then becomes

$$\begin{aligned}
-\frac{\mathrm{d}E}{\mathrm{d}x} &= K\frac{Z}{A}\frac{1}{\beta^2}\left[\frac{1}{2}\ln\left(\frac{\tau^2(\tau+2)m_e^2c^4}{2I^2}\right)-\frac{F(\tau)}{2}-\frac{\delta(\beta\gamma)}{2}-\frac{C}{Z}\right],\\
F(\tau) &= 1-\beta^2+\frac{\tau^2/8-(2\tau+1)\ln(2)}{(\tau+1)^2} \quad \text{for electrons},\\
F(\tau) &= 2\ln(2)-\frac{\beta^2}{12}\left[23+\frac{14}{\tau+2}+\frac{10}{(\tau+2)^2}+\frac{4}{(\tau+2)^3}\right] \quad \text{for positrons}, \qquad (6)
\end{aligned}$$

where $\tau = \gamma - 1$ represent the kinetic energy of electrons divided by m_ec^2.

Bremsstrahlung

When electron (or positron) energies exceed a few tens of MeV, radiative energy loss, *i.e.* the emission of photons, becomes the dominant mechanism. This emission is usually referred to as synchrotron radiation, when it is due to a magnetic field bending, as it occurs in circular accelerators, or as bremsstrahlung (braking radiation in German) when traversing matter. Bethe and Heitler were the first to derive a quantum-mechanical calculation of the bremsstrahlung emission by an electron in the field of a heavy, point-like and spin-less nucleus [22]. A more recent treatment of bremsstrahlung and pair-production has been derived [25] in the frame of quantum field theory. In a far from rigorous way, we can derive this behaviour with a heuristic reasoning assuming that acceleration is uniform during the radiative diffusion.

We can then evaluate the radiated power as a classical electromagnetic-dipole radiation emission

$$\frac{\mathrm{d}E}{\mathrm{d}t} = \frac{2}{3}\frac{e^2a^2}{c^3} \propto \frac{z^2Z^2}{m_e^2} \tag{7}$$

which depends quadratically on the square of the acceleration.

The acceleration used in Eq. (7) is the ratio of the electrostatic force between the nucleus of charge Ze and the electrons, and the electron mass. As a consequence, the bremsstrahlung intensity depends inversely on the square of the incoming particle mass, therefore, it is much less probable that a massive charged particle (μ, π, K, proton, *etc.*) radiates photons traversing a medium than an electron or a positron. In addition, while ionisation loss rates rise logarithmically with energy, bremsstrahlung losses rise nearly linearly (fractional loss k is nearly independent of energy, *i.e.* $\Delta E \propto kE$), and dominate above the critical energy, which is a few tens of MeV in most materials for electrons/positrons.

Several definitions of the critical energy E_C exist. The most natural is the one which identifies the E_C as the energy at which bremsstrahlung loss equals ionisation loss [26], for which Bethe and Heitler [22] gave a first approximation formula, later improved by Amaldi [27]. A less recent but more accurate formula was given by Dovzhenko and Pomanskii [28] ($B = 2.66$, $h = 1.1$). An alternative definition is due to Rossi [29] who defines the critical energy as the energy at which the ionisation loss per radiation length is equal to the electron energy

$$E_\mathrm{C} = \frac{1600\, mc^2}{Z} \quad (\text{Bethe–Heitler})\,, \tag{8}$$

$$E_\mathrm{C} = \frac{550}{Z}\ \mathrm{MeV} \quad (\text{Amaldi})\,, \tag{9}$$

$$E_\mathrm{C} = \frac{800}{Z+1.2}\ \mathrm{MeV} \quad (\text{Berger and Seltzer})\,, \tag{10}$$

$$E_\mathrm{C} = B\left(\frac{ZX_0}{A}\right)^h \quad (\text{Dovzhenko–Pomanskii})\,, \tag{11}$$

$$E_\mathrm{C} = E_e = \frac{1}{X_0}\left\langle\frac{\mathrm{d}E}{\mathrm{d}x}\right\rangle \quad (\text{Rossi})\,. \tag{12}$$

Here, we will adopt the Rossi definition as this form has been found to describe more accurately the transverse electromagnetic shower development discussed later on. It is worth to note that a good approximation for E_C can be obtained from the empirical formula

$$E_\mathrm{C}^{\mathrm{gas}} = \frac{710\ \mathrm{MeV}}{Z+0.92}\,, \qquad E_\mathrm{C}^{\mathrm{sol/liq}} = \frac{610\ \mathrm{MeV}}{Z+1.24}\,. \tag{13}$$

The spectrum of photons emitted by bremsstrahlung can be expressed as a function of the particle energy E and the photon energy k, $y = k/E$

$$\frac{\mathrm{d}\sigma}{\mathrm{d}k} = 4\alpha Z(Z+1)r_e^2 \ln\left(\frac{183}{Z^{1/3}}\right)\left(\frac{4}{3} - \frac{4}{3}y + y^2\right)\frac{1}{k}\,. \tag{14}$$

The term $Z(Z+1)$ is due to the coupling of the impinging electron with the EM field of the nucleus, increased by the direct contribution of the atomic electrons (which was simply Z^2 in the Bethe–Block). The term $183\ Z^{-1/3}$ takes into account the screening of the nucleus field by the atom's electrons. By integrating Eq. (14) over y we can obtain the energy loss for bremsstrahlung

$$\frac{\mathrm{d}E}{\mathrm{d}x} = 4\alpha N_A Z^2 r_e^2 \ln\left(\frac{183}{Z^{1/3}}\right) E\,. \tag{15}$$

It is worth to note that the energy loss is proportional to the inverse of the square of the mass, as shown in Eq. (7). An important quantity in describing this phenomenon is the radiation length X_0, which is the mean distance over which a high-energy electron loses all but $1/e$ of its energy by bremsstrahlung and it is also related to mean interaction length $\lambda_{\mathrm{int}} = 9X_0/7$ for pair-production by a high-energy photon. From Eq. (15), using the definition of energy, we obtain

$$\frac{\mathrm{d}E}{\mathrm{d}x} = \frac{E}{X_0} \Longrightarrow X_0 = \left[4\alpha N_A Z^2 r_e^2 \ln\left(\frac{183}{Z^{1/3}}\right)\right]^{-1}\,. \tag{16}$$

2.1.3. Interaction of photons with matter

The interaction of photons with matter is substantially different from what happens with charged particles. As a matter of fact, a photon is either absorbed or scattered when traversing a slab of material. Thus, a fraction $\mathrm{d}N$ of the initial N_0 photons are removed from a beam when traversing a slab $\mathrm{d}x$ of material

$$\mathrm{d}N = -\mu N \mathrm{d}x \Longrightarrow N(x) = N_0\,\mathrm{e}^{-\mu x} = N_0\,\mathrm{e}^{-x/\lambda}\,, \tag{17}$$

where the quantity μ is the attenuation coefficient and λ is the attenuation length, or the interaction length, as defined in Eq. (2), which connect the probability of interaction with the cross section. In the case of the photons, three main processes contribute to the total cross section. In the photo-electric effect, the photon is absorbed by an atomic electron of the outer shells, which is then ejected from the atom. The Compton scattering is a quantum phenomenon that can be schematised as an elastic scattering of a high-energy photon by an electron of the atoms, which is considered quasi-free as the photon energy is higher than the binding energy.The pair-production is the creation of an electron–positron pair by a photon, with an energy greater than $2m_e$ in the Coulomb field of an electron or a nucleus. As shown in Fig. 6, as soon as the energy reaches the threshold for the pair-production, $E > 1.02$ MeV, this phenomenon becomes the dominant one in the total cross section. At energies below this threshold, instead, the total cross section is a convolution of the photo-electric effect and the Compton scattering depending on the material, given the different dependence of the cross sections from the Z of the material. As a matter of fact, the photo-electric cross section σ_{ph} scales as Z^5, while the Compton scattering σ_{Comp} scales as Z. This is clearly visible in Fig. 6 where for lead the σ_{ph} is dominant over the Compton until the pair-production takes over. For lighter material as carbon, the Compton starts to emerge between the photo-electric and the pair-production. This explains why high-Z materials are used, in general, for calorimeters in high-energy physics. Not only the stopping power is high, but also it minimises the Compton scattering and enhances the photoelectric absorption of photons, which can be converted into a signal.

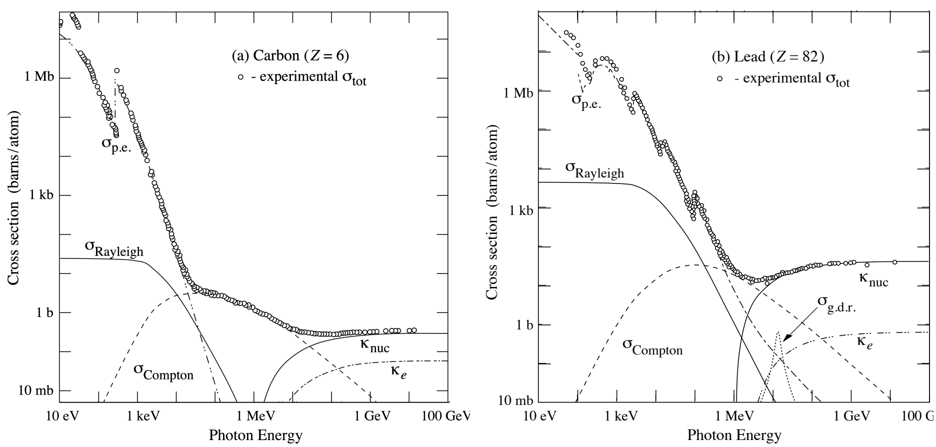

Fig. 6. Total cross section for photons as a function of energy for carbon (left) and lead (right).

The pair-production cross section σ_{pair} can be written as a function of $x = E/k$, where E and k are, as before, the energy of the electrons and the photon, respectively

$$\frac{\mathrm{d}\sigma_{\text{pair}}}{\mathrm{d}x} = \frac{A}{X_0 N_A}\left(1 - \frac{4}{3}x(x+1)\right) \Longrightarrow \sigma_{\text{pair}} = \frac{7}{9}\frac{A}{X_0 N_A} \tag{18}$$

from which we can derive the interaction length $\lambda_{\text{int}} = 1/(N\sigma_{\text{pair}}) = 9X_0/7$.

2.2. Electromagnetic showers

The bremsstrahlung and the pair-production are the main actors in the development of electromagnetic (EM) showers, a cascading effect, which generates a "shower" of electrons and photons in the material. It is customary the fact that both phenomena are related to the radiation length X_0. The electromagnetic shower is a pure EM process involving only electrons/positrons[4] and γ interaction with matter. The gammas can produce particle via pair-production, while e can emits photons via bremsstrahlung. The process is then a kind of chain reaction in which at each step e and γ converts one into the other and stops when the energy of the e is below the critical energy and/or the photons energy is below the pair-production and they are absorbed. Though a statistical process is governed by the relative cross sections, a simplified model can quite well describe the main characteristics of this showers, such as number of particles in the shower, the location of the shower maximum $X_{\rm max}$, the shower profile. Heitler developed a model for the shower development that under very general assumption is capable of describing the shower main features. The basic assumption is that at each stage i (after one X_0), a parent i produces 2 children, equally sharing the energy, *i.e.* each one has $E_{i+1} = E_i/2$.

Thus, after t stages, the number of particles is $N(t) = 2^t$, each with an energy $E_t = E_0/N(t) = E_0 \times 2^{-t}$. The shower will reach is maximum when $E_{t_{\rm max}} = E_{\rm C}$

$$t_{\rm max} = \frac{\ln(E_0/E_{\rm C})}{\ln 2} \propto \ln(E_0)\,, \tag{19}$$

$$N_{\rm max} = \frac{E_0}{E_{\rm C}} \Longrightarrow X_{\rm max} = X_0 \ln\left(\frac{E_0}{E_{\rm C}}\right)\,. \tag{20}$$

From Eq. (20), we can see that the shower maximum increases as $\ln(E_0)$ of the energy of the primary particle which started the shower but also the shower development starts to have a longer tail as shown in Fig. 7. The longitudinal profile of the shower in an electromagnetic calorimeter has been parametrised as a function of the depth t as $\mathrm{d}E/\mathrm{d}t = E_0\, t^\alpha\, \mathrm{e}^{-\beta t}$ [30].

The first term t^α reflects the fact that at early stage, the number of secondaries grows fast, while the second term $\mathrm{e}^{-\beta t}$ describes the final stages when absorption starts to dominate. For a 2 GeV electrons, typical values are $\alpha = 2$ and $\beta = 0.5$, while $t_{\rm max} = \alpha/\beta$.

A more precise parametrisation was given later [31]

$$\frac{\mathrm{d}E}{\mathrm{d}t} = E_0\, \beta \frac{(\beta t)^{\alpha-1}\, \mathrm{e}^{-\beta t}}{\Gamma(\alpha)} \quad \Longrightarrow \quad t_{\rm max} = \frac{\alpha - 1}{\beta} = \ln\left(\frac{E_0}{E_{\rm C}}\right) - C_{e\gamma}\,, \tag{21}$$

where $C_{e\gamma} = 1$ for e-induced shower and $C_{e\gamma} = 0.5$ for γ-induced shower.

[4] We will in the following use e to identify simultaneously electrons and positrons.

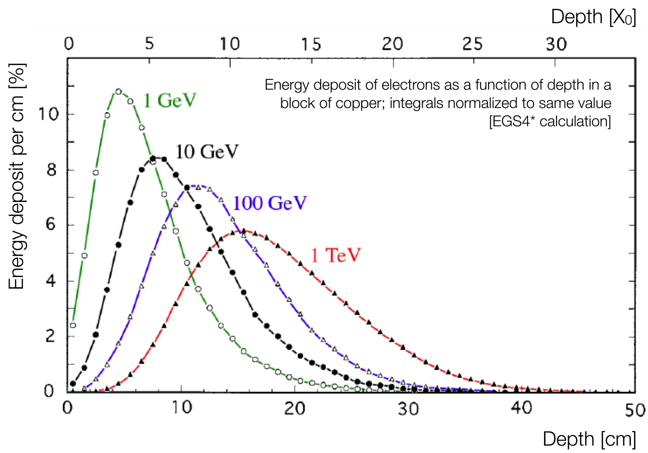

Fig. 7. Simulation of energy deposit for an electron with different energies as a function of the depth in a block of copper. To compare the profile, the curve integrals are normalised to the same value. The vertical scale gives the energy deposit as fraction of the initial energy E_0. The simulation was performed with EGS4 code.

The transverse shower profile is dominated by the multiple scattering suffered by electrons and positrons, and scales fairly accurately with the *Molière radius*, which has the dimension of a radiation length and is characteristic for the medium in which the shower develops. Its value, for most of materials, is close to 14 g/cm^2/density. A good approximation, valid in most of the casesis [23]

$$R_{\mathrm{M}} = X_0 \frac{E_{\mathrm{s}}}{E_{\mathrm{C}}} \approx 21.2 \text{ MeV} \frac{X_0}{E_{\mathrm{C}}}\,, \qquad E_{\mathrm{s}} = \sqrt{\frac{4\pi}{\alpha}} m_e c^2 = 21.2 \text{ MeV}\,. \quad (22)$$

In electromagnetic showers, 90% and 95% of the energy is deposited within one and two Molière radii, respectively.

2.3. Hadronic shower

Hadrons undergo mainly strong interaction when traversing matter. In this case, many more diverse processes are involved with respect to the case of the EM shower and, in addition, in some cases the energy transferred cannot be detected. The high-energy hadrons undergo both elastic and inelastic scattering and the total cross section is $\sigma_{\mathrm{tot}} = \sigma_{\mathrm{el}} + \sigma_{\mathrm{inel}}$. The hadronic cross section is fairly independent of energy and hadron type. The elastic cross section is of the order of $\sigma_{\mathrm{el}} \approx 10$ mbar, but the inelastic dominates already for hadrons with few GeV of energy. The inelastic cross section for a hadron impinging on a material of atomic mass A can be approximated by the simple form as

$$\sigma_{\mathrm{inel}}(p,A) \simeq \sigma_{\mathrm{inel}}^{pp} \times A^{2/3}\,, \tag{23}$$

where $\sigma_{\mathrm{inel}}^{pp} = 35$ mb is the proton–proton inelastic cross section. We can then define an interaction length for hadronic interaction

$$\lambda_{\mathrm{int}} = \frac{A}{N_A\,\sigma_{\mathrm{inel}}(P,A)} \simeq 35\ A^{1/3}\ \mathrm{g\,cm}^2\,. \tag{24}$$

The definition in Eq. (24) is an approximation, as we should have used the total cross section, but as noted before the inelastic is the dominant.

Hadrons produce a flow of particles while traversing a material as a result of complex and diverse interactions, which makes the shower development not only more complex but also more prone to the statistical fluctuations.

As a matter of fact, together with production of secondary with typical momentum of GeV, a non-negligible fraction (up to 50%) of the primary energy is diverted into nuclear processes such as excitation, nucleon evaporation, spallation, *etc.* which results in particle either of very small energy (below MeV) or undetectable (neutrinos, phonons, *etc.*), as reported in Table I. In addition, the contributions of the different phenomena depend on the material.

TABLE I

Breakdown in the different component of the energy loss for a pion of 5 GeV.

Ionisation energy of charged particles	1980 MeV	40%
Electromagnetic shower	760 MeV	15%
Neutrons	520 MeV	10%
Photons from nuclear de-excitation	310 MeV	6%
Non-detectable (nuclear binding, neutrinos)	1430 MeV	29%
Total	5000 MeV	

All the undetectable components of the hadronic shower cause the problem of the non-compensation in calorimeter, *i.e.* a different response with large fluctuations for particles with the same energy, depending if they undergo the EM (e) or hadronic (h) interaction. Thus, in general, the calorimeter signals for hadrons are smaller than for electrons of the same energy. In a general purpose experiment, the calorimetry is done having a first stage with an EM calorimeter and a second stage with a hadronic calorimeter. In many cases, a particle traverses both calorimeters and then its energy is a combination of the two pieces of information. In general, the ratio e/h is different from unity. The fraction of energy lost in EM shower is usually referred to as f_{em}, which is energy-dependent and has large and non-Poissonian event-to-event fluctuations.

For pions, which represent a big component of the hadronic shower, as an example we have that the total energy can be written as $\langle f_{\rm em}\rangle + e/h\,(1-\langle f_{\rm em}\rangle)$. This energy is then largely fluctuating leading to a non-linear response for hadrons. We can, anyhow, try to model the shower process also for hadrons. It is important to note that the vast majority of secondaries produced are pions (90%). The neutral pions decay into two gammas, and then can start an EM shower. The fraction of the shower energy carried by this EM component $\langle f_{\rm em}\rangle$ on average increases with the shower energy, since π^0 may also be produced by secondary and higher-order shower particles. Therefore, the larger is the shower energy, the more generations of shower particles are produced and the larger is $\langle f_{\rm em}\rangle$. We can try to build a simple model assuming that pions are the dominant components and then 1/3 of the energy goes into EM shower started by π^0, *i.e.* $\langle f_{\rm em}\rangle = 1/3$. Under this assumption, after n stages of development of the shower $\langle f_{\rm em}\rangle = 1 - (1-1/3)^n$. The factor 1/3 is a too rough approximation and, in truth, we need to use an average multiplicity $\langle m\rangle$ per interaction. In this case, $\langle f_{\rm em}\rangle = 1-(1-1/\langle m\rangle)^n$.

Typically, $\langle f_{\rm em}\rangle$ increases from 30% at 10 GeV to 50% at 100 GeV. For dense materials, it has been shown [32, 33] that $\langle f_{\rm em}\rangle = 1-(E/E_0)^{(k-1)}$ (see Fig. 8). It is possible to make a simplified model based on the same approach of the EM showers by adopting a different scale $\lambda_{\rm int}$, which plays the same role of X_0 in EM showers. Let us define the shower depth as $t = x/\lambda_{\rm int}$ and define an energy threshold $E_{\rm thr} \approx 290$ MeV with the same role of $E_{\rm C}$ for EM showers. We can then define in analogy with EM showers

$$E(t) = \frac{E}{\langle n\rangle^t} \Longrightarrow E_{\rm thr} = \frac{E}{\langle n\rangle^{t_{\max}}}\,, \tag{25}$$

$$\langle n\rangle^{t_{\max}} = \frac{E}{E_{\rm thr}} \Longrightarrow t_{\max} = \frac{\ln(E/E_{\rm thr})}{\ln\langle n\rangle}\,. \tag{26}$$

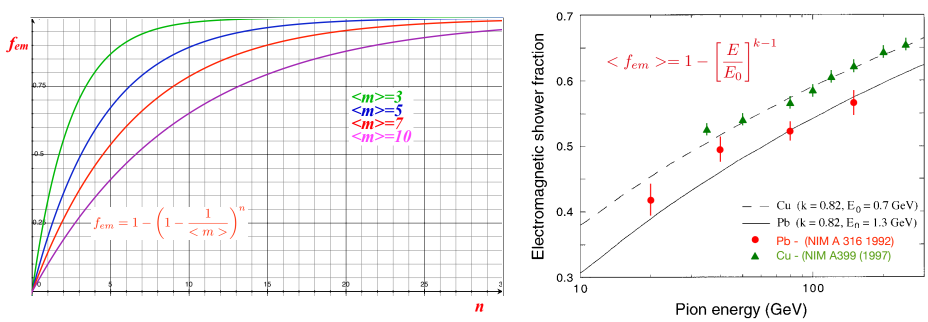

Fig. 8. Electromagnetic fraction $\langle f_{\rm em}\rangle$ of hadronic shower. The dependence of $\langle f_{\rm em}\rangle$ from the pion multiplicity on the left and as a function of the pion energy for lead and copper (right).

This model is just useful to have a rough picture of the hadronic showers and helps in deriving some trend for the main quantities, while the event-to-event fluctuations are significant and then the Monte Carlo simulation is needed for a quantitative analysis of the shower.

As we have shown before, the dependence of X_0 from the material is $X_0 \sim A/Z^2$, while for $\lambda_{\rm int} \sim A^{\frac{1}{3}}$ and then $\lambda_{\rm int}/X_0 \sim A^{\frac{4}{3}}$.

As shown in Fig. 9 (left), $\lambda_{\rm int}$ is much larger than X_0. This is used in many experiments to distinguish between electrons and hadrons on the basis of the energy deposit profile and signal shape in their calorimeter system.

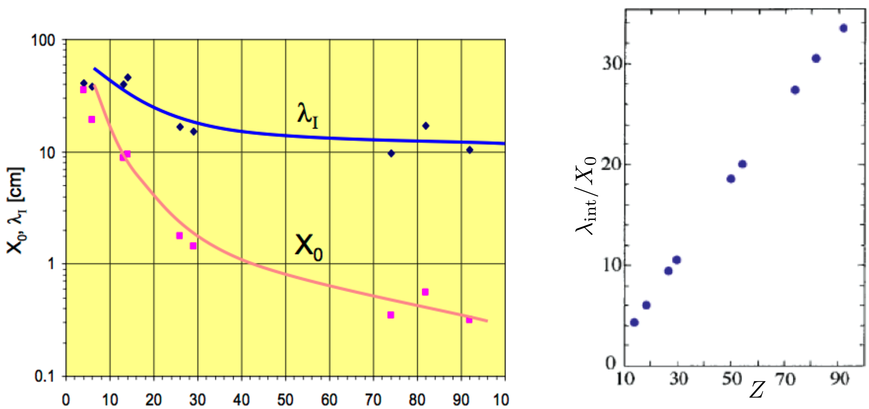

Fig. 9. Dependence of $\lambda_{\rm int}$ and X_0 from the material Z on the left. Dependence of the ratio $\lambda_{\rm int}/X_0$ from Z on the right.

Moreover, as can be seen in Fig. 9 (right), the ratio $\lambda_{\rm int}/X_0$ is proportional to Z and then a particle identification based on this difference works better for high-Z absorber materials. It is worth to mention here that, similarly to what happens for EM showers in which the 95% shower transversal development is contained in a cone of dimension of $R_{\rm M}$, also for hadrons the shower is contained in $R_{95\%} \approx \lambda_{\rm int}$ [27, 34]. The hadronic lateral spread is due mostly to the secondaries produced at large angles, with typical transverse momentum of $\langle p_{\rm t} \rangle \sim 350$ MeV. The shower EM component leads to a relatively well-defined core $R = R_{\rm M}$, which after the shower maximum experience an exponential decay. Energetic neutrons and charged pions form a wider core and the thermal neutron generates a broad tail. The containment of the longitudinal development of hadronic shower $L_{95\%}$, which corresponds to the absorber depth at which 95% of the shower energy is deposited, is to a first approximation described by [16]

$$L_{95\%} = t_{\rm max} + 2.5\,\lambda_{\rm int}\,, \quad \text{where} \quad t_{\rm max} \approx 0.2\,\ln(E\ \text{GeV}) + 0.7\,. \tag{27}$$

We described so far the main processes and quantities used in calorimetry for high-energy physics, but for cosmic-ray physics, the energies are much higher, and some different phenomena enter into the game.

2.4. Characteristics of air showers

The cosmic rays (CRs), high energy particles or gammas, impinge on the atmosphere and interact with its atoms producing shower exactly like in a calorimeter.

For a vertical shower, the atmosphere is a calorimeter of about 26 X_0 and 15 λ_{int}, which is not much different from the ATLAS calorimeter with its 27 X_0 and 11 λ_{int}. At the same time, the atmosphere is a strongly inhomogeneous material and its density, and then X_0, varies with the altitude and atmospheric conditions (pressure, temperature, humidity, *etc.*).

2.4.1. Electromagnetic air showers

The model for EM shower discussed so far is still applicable for air shower. As a matter of fact, the atmosphere can be assimilated to a chemical element with a $Z = 7$, which yield a critical energy $E_{\mathrm{C}} = 580$ MeV$/Z$. The density of air diminishes by six orders of magnitude when the altitude goes from the sea level (~ 1.0 kg/cm^2, $X_0 = 300$ m) up to 100 km, and another six orders from 100 to 300 km. Many models exist and have been used/developed by the experiment (HESS, VERITAS, AGASA, Pierre Auger, HiRes). Despite the atmosphere being a strongly inhomogeneous medium, under the quite general assumption of isothermal atmosphere, many characteristics of the shower and the primary producing them can be reconstructed as we will show later.

At the same time, under very extreme conditions, such as extremely high energies or extremely high magnetic fields, or in a combination of both, some peculiar processes and phenomena occur. Particularly relevant for ultra-high energy photons and electrons showers development are the Landau–Pomeranchuk–Migdal (LPM) effect and the magnetic bremsstrahlung and pair-production.

2.4.2. Landau–Pomeranchuk–Migdal effect

At ultra-high energies, the quantum mechanical interference between amplitudes from different scattering centres starts to become relevant in both the pair-production and bremsstrahlung . This interference is usually destructive and, therefore, suppress the cross sections. This effect is named the Landau–Pomeranchuk–Migdal (LPM) after the names of the three scientists who calculated the effect on the cross section. While Landau and Pomeranchuk [35] calculated the effect with a semi-classically approach based on the average multiple scattering, Migdal [36] was the first one to make a more rigorous calculation using a quantum transport approach. More details can be found in a more recent review by Klein [37]. The consequence of the LPM effect is to slow down the rate of the initial phase of an electromagnetic shower initiated by an ultra-high energy photon or electron, which then can penetrate deeper into the medium and the shower is stretched at the beginning. The cross section for bremsstrahlung of electrons in Eq. (14) is shown in Fig. 10.

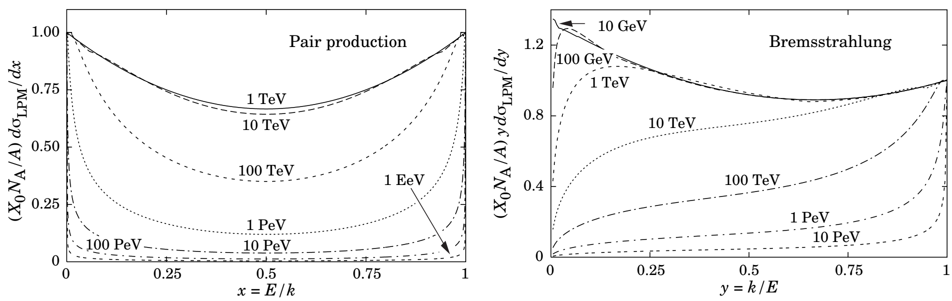

Fig. 10. The cross section for pair-production (left) and bremsstrahlung (right) as a function of the ratio $x = E/k = 1/y$, where E is the electron energy and k the gamma momentum.

The phenomenon is linked to the fact that bremsstrahlung is not a single point interaction but has to deal with an effective region where bremsstrahlung and pair-production happen in the vicinity of a nucleus. The radius of this region, which represents the effective average collision distance from nucleus, is given by the uncertainty principle [38]

$$r_{\text{eff}} \sim \frac{\hbar c}{q_{\parallel}} \sim \frac{E(E-k)}{m_e c^2 k}\left(\frac{\hbar}{m_e c}\right), \tag{28}$$

where E is the energy of the incident electrons, k the energy of outgoing photon, and the longitudinal momentum transfer to a given center is

$$q_{\parallel} \sim \frac{m_e^2 c^4 k}{2E(E-k)} \quad \text{for} \quad (E-k) \gg m_e c^2\,. \tag{29}$$

Therefore, for small momentum $q_{\parallel}$, the interaction is spread over a comparatively long distance r_{eff} called the formation length. In other words, the formation length is the distance over which the highly relativistic electron and the photon split apart. In amorphous media, the bremsstrahlung is suppressed by the multiple scattering $\langle\vartheta^2_{\text{MS}}\rangle$ of the electron when it dominates over the transverse momentum

$$\sqrt{\langle\vartheta^2_{\text{MS}}\rangle} > \frac{m_e c^2}{E}\,, \quad \text{where} \quad \langle\vartheta^2_{\text{MS}}\rangle \sim \left(\frac{E_{\text{scatt}}}{E}\right)^2\left(\frac{r_{\text{eff}}\rho}{X_0}\right), \tag{30}$$

where we used X_0/ρ as here we are comparing lengths. By using Eqs. (28) and (29), the condition becomes

$$\frac{E(E-k)}{k} > \frac{m_e^4 c^7}{\hbar E_{\mathrm{scatt}}^2}\frac{X_0}{\rho} = E_{\mathrm{LPM}} = 7.7\left[\frac{\mathrm{TeV}}{\mathrm{cm}}\right]\frac{X_0}{\rho}\,. \tag{31}$$

The dependence from X_0 makes the LPM effect most significant in heavy elements at very high energy. It is worth to note that the dependence from m_e^4 is such that already for muons LPM suppression is generally negligible for both muon bremsstrahlung and pair creation ($E_{\mathrm{LPM}}^{\mu} = 1.38 \times 10^{10}$ TeV/cm $\frac{X_0}{\rho}$). The bremsstrahlung spectrum energy-weighted $k\mathrm{d}\sigma_{\mathrm{LPM}}/\mathrm{d}k$ is shown in Fig. 10 (right) for lead, but other materials behave similarly, with appropriate scaling by X_0/ρ. For photons, instead, the pair-production cross section is reduced for $E(E-k) > E_{\mathrm{LPM}}$ and in Fig. 10 (left), it is shown for different photon energies. In crystalline media, the situation is more complicated as the cross section depends on the electron and photon energies and the angles between the particle direction and the crystalline axes, which can produce both coherent enhancement and suppression. The first tests of LPM suppression came quite shortly after Migdal paper in cosmic ray physics, where the depth of pair conversion in a dense target high-energy ($k > 1$ TeV) photons was studied. Many others followed but the poor statistics and uncertainties in the photon spectrum complicated the analysis. A clear prove of the effect was possible only with particle collider later on. In particular, in 1992, the E-146 Collaboration at the Stanford Linear Accelerator Center (SLAC) proposed an experiment to perform a precision measurement of LPM suppression and to study dielectric suppression [39].

2.4.3. Geomagnetic pre-showering

If an ultra-high energy photon approaching the Earth interacts with the geomagnetic field, even far beyond the fringes of the atmosphere, it can cause magnetic electron pair-production and, subsequently, these newly created electrons undergo themselves magnetic bremsstrahlung. This sequence of elementary processes may repeat itself several times before reaching the atmosphere, thus provoking a small but very energetic highly collimated shower. In Fig. 11 is shown the conversion probability (left) and the height of first conversion (right). This process, known as pre-showering, may mimic the arrival of a single heavy primary, such as iron, generating an iron-like shower upon entry into the atmosphere of these groups of particles. It is then a major problem for primary mass determination at the highest energies ($> 10^{18}$ eV). The magnetic bremsstrahlung and pair-production are governed essentially by a single parameter Υ [38]

$$\Upsilon = \left(\frac{E}{m_e c^2}\right)\left(\frac{H_\perp}{H_{\mathrm{crit}}}\right), \quad \text{where} \quad H_{\mathrm{crit}} = \frac{m_e^2 c^3}{e\hbar} = 4.414 \times 10^{13}\ \mathrm{G}\,. \tag{32}$$

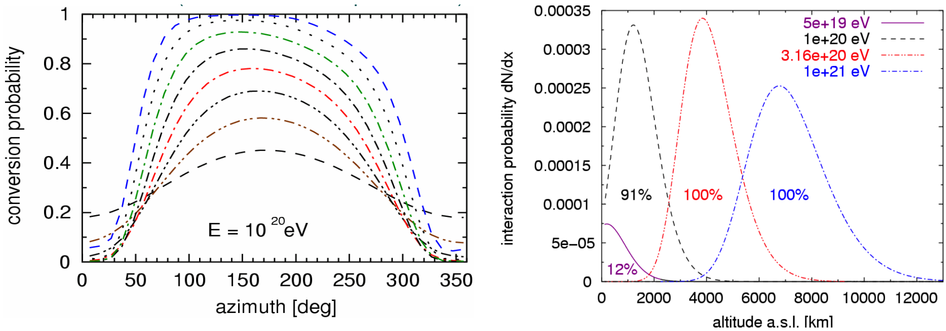

Fig. 11. Geomagnetic pre-showering. Left: Total probability of gamma conversion for different arrival directions. Each curve corresponds to a different zenith angle: $\vartheta = 80°$ for the uppermost curve down to $\vartheta = 0°$ for the lowest one in steps of $10°$. Right: Altitudes of first conversion along strong field direction for four different primary photon energies.

It is possible to define a critical energy $E_M^{\rm crit}$ which represents the threshold that a particle must exceed for the process to become effective and that plays essentially the same role as the critical energy in an ordinary electromagnetic cascade

$$E > E_M^{\rm crit} = m_e c^2 \left(\frac{H_{\rm crit}}{H_\perp}\right) . \tag{33}$$

The main characteristics of a shower initiated in a strong magnetic field in vacuum can be described by formulae that are entirely analogous to those for showers but replacing the radiation length by an *effective radiation length* $L_{e,\gamma}$ both for electrons and photons. However, a fundamental difference lies in the fact that the radiation length in a magnetic field in vacuum is energy-dependent and extremely small (short)

$$L_{e,\gamma} \sim K_{e,\gamma} \left(\frac{E_0}{\rm GeV}\right)^{1/3} \left[3.9 \times 10^6 \left(\frac{H_\perp}{H_{\rm crit}}\right)\right]^{-1} \ {\rm cm}\,. \tag{34}$$

What is interesting about the two above-mentioned process is the fact that they affect only electrons and gammas and not hadrons, given their higher mass. So as said before, the suppression allows gammas to enter more in depth in the atmosphere, and then their measured $X_{\rm max}$ is larger than the corresponding one for hadrons with the same energy. At ultra-high energy, $X_{\rm max}$ can be of the order of several hundreds of ${\rm g\,cm}^2$ and allows a good separation. Unfortunately, the low statistics at that energies and the limited energy resolution do not allow to prove this effect or use it to improve identification of primary particle.

In the EM shower model discussed before, the basic assumption was that at each stage, the particle number doubles and the process starts to fade once electrons reach the critical energy and begin to be absorbed. This has been revisited in case of air shower. In air, the critical energy is $E_{\mathrm{C}}^{\mathrm{air}} \simeq 85$ MeV and, if $N_{\max}$ is the maximum number of particles, the energy of the primary is $E_0 = N_{\max} E_{\mathrm{C}}^{\mathrm{air}}$. The number of stages t after which the shower reaches its maximum can be derived from $N_{\max} = 2^t$, where $t = \ln\left(E_0/E_{\mathrm{C}}^{\mathrm{air}}\right)/\ln(2)$. The maximum penetration depth, where the shower reaches its maximum, is then $X_{\max} = t\,\lambda_{\mathrm{int}}\,\ln(2) = \lambda_{\mathrm{int}}\,\ln\left(E_0/E_{\mathrm{C}}^{\mathrm{air}}\right)$.

The rate of increase of $X_{\max}$ with E_0 is called the elongation rate

$$\Lambda \equiv \frac{\mathrm{d}X_0}{\mathrm{d}\log_{10}E} = \frac{\lambda_{\mathrm{int}}}{\log(e)} = 2.3\lambda_{\mathrm{int}} \simeq 85\ \mathrm{g\,cm^{-2}}\,. \tag{35}$$

This model overestimates $N_{\max}$ and the actual ratio of electrons to photons, which is predicted to reach $N_e \approx 2/3 N_{\max}$. One reason is that multiple photons are often radiated during bremsstrahlung, therefore, the number of photons greatly out-numbers electrons throughout the development of the shower. The number of photons can be up to six time larger than electrons at their respective maximum. In truth, after the shower maximum, there are many other processes to take into account for modelling shower in more detail, but it is far beyond the scope of what is discussed here. The maximum number of electrons is an order of magnitude less than what the Heitler model predicted. Matthews [40] proposed to use a correction factor g to recover the correct number of electrons $N_e = N/g$. For many cases, $g = 10$ is used, but often g is tuned using actual experiment measurements. In any case, the model reproduces two main features of the shower, *i.e.* the maximum size of the shower proportional to E_0 and the logarithmic increase of the depth of maximum at a rate of 85 $\mathrm{g\,cm^2}$ per decade of primary energy.

2.4.4. Hadronic air showers

High-energy hadronic particles, entering the Earth's atmosphere, produce showers interacting with nuclei from the air (mainly nitrogen, oxygen, and argon) at a typical height between 15 and 35 km. The most frequently produced secondary hadrons are charged and neutral pions. While neutral pions ($c\tau = 25$ nm) immediately decay into two photons starting EM showers, charged pions ($c\tau = 7.8$ m) interact again before decaying into muons, once they have reached a critical energy $E_{\mathrm{C}}^{\pi} \sim 20$ GeV. Charged kaons decay at higher energies given the slightly shorter lifetime ($c\tau = 3.7$ m). The hadronic shower core is formed by these long-lived secondary hadrons (baryons, charged pions, and kaons), whose decays produce almost 90% of the muons in the shower, which propagate through the atmosphere with small energy losses and reach the surface of the Earth almost unattenuated.

In showers with very large zenith angles ($\vartheta > 65^{\circ}$), this muonic shower component and the EM particles produced in the decay of muons are the only particles that can be detected at the ground. In this scheme, the primary particle energy will be divided between N_{π} and $N_{\max}$ electromagnetic particles. For what was said before, the number of muons is $N_{\mu} = N_{\pi}$ and then $E_0 = E_{\rm C}^{e} N_{\max} + E_{\rm C}^{\pi} N_{\mu}$. Assuming a standard parametrisation [40] ($E_{\rm C}^{\pi} = 20$ GeV, $E_{\rm C}^{\rm e} = 85$ MeV, $g = 10$) and recalling that $N_{\max} = gN_e$, we have

$$E_0 = gE_{\rm C}^{e}\left(N_e + \frac{E_{\rm C}^{\pi}}{E_{\rm C}^{e}}\frac{N_{\mu}}{g}\right) \approx 0.85 \text{ GeV } (N_e + 24N_{\mu})\,. \tag{36}$$

The importance of Eq. (36) lies in the fact that E_0 is simply calculable by measuring N_e and N_{μ}. As a matter of fact, different primaries energy will distribute differently between the electromagnetic and hadronic components, as do statistical fluctuations, but Eq. (36) implicitly accounts for this, being linear in N_e and N_{μ}, and then insensitive both to fluctuations and to primary particle type. Clearly, the measurement of $N_{e,\mu}$ depends on the experimental detail and then the coefficients in Eq. (36) need some tuning. For example, for the CASA-MIA experiment [41], it was found a good agreement with data with $E_0 = 0.80(N_e + 25N_{\mu})$. The number of pions, and then of muons, is related to their critical energy as [42, 43]

$$N_{\mu} = \left(\frac{E_0}{E_{\rm C}^{\pi}}\right)^{\beta} \approx 10^4 \left(\frac{E_0}{1 \text{ PeV}}\right)^{\beta}, \quad \text{where} \quad \beta = 0.85 \ \ldots \ 0.92\,. \tag{37}$$

To estimate the number of electrons, we can use the fact that $E_0 = E_{\rm em} + E_{\rm h}$, and using Eq. (37) with a series of approximations in the region of interest of $E_0 = 10^6\ E_{\rm C}^{\pi}$, it can be shown to be [40]

$$N_e = \frac{1}{g}\frac{E_{\rm em}}{E_{\rm C}^{\pi}} \approx 10^6 \left(\frac{E_0}{1 \text{ PeV}}\right)^{\alpha}, \quad \text{where} \quad \alpha = 1 + \frac{1-\beta}{10^{5(\beta-1)} - 1} \approx 1.03\,. \tag{38}$$

This can be inverted to give $E_0 = 1.5$ [GeV]$N_e^{0.97}$ in good agreement with full simulation [42], which gives $E_0 = 1.6$ [GeV]$N_e^{0.99}$. Thus, a measurement of N_e at shower maximum can give a measure of the energy of the primary.

So far, we have always discussed primary particles, but we know that cosmic rays are also nuclei. All arguments discussed so far and the model of shower can still be applicable thanks to the *superposition model*, which considers a nucleus of mass A with energy E_0 as A independent nucleons (protons) each with energy E_0/A. This is an approximation, which though crude, is anyhow reasonable, given that the binding energy is small compared to interaction energies. Thus, for a nucleus A, thanks to the superposition model, we can write

$$
\begin{aligned}
N_{\max}^{A}(E_0) &= A N_{\max}^{p}(E_0/A) \simeq N_{\max}^{p}(E_0)\,, \\
X_{\max}^{A}(E_0) &= X_{\max}^{p}(E_0/A)\,, \\
N_{\mu}^{A}(E_0) &\approx A\left(\frac{E_0/A}{E_{\mathrm{C}}^{\pi}}\right)^{\beta} = A^{(1-\beta)} N_{\mu}^{p}(E_0)\,.
\end{aligned} \tag{39}
$$

It is important to note that while the number of charged particles $N_{\max}$ at shower maximum is almost independent of the type of nucleus, the number of muons N_μ and the depth of maximum $X_{\max}$ depend on the mass of the nucleus. In addition, the heavier is the nucleus, the more muons are expected for a given primary energy. For example, for iron with $A = 56$ and $\beta = 0.92$, the showers contain about 40% more muons than proton showers of the same energy and its maximum is 80–100 g/cm^2 higher in the atmosphere. The superposition model gives a good description of many features of air showers, the mean depth of shower maximum or the number of muons, but in general only for all-inclusive observables. As a matter of fact, the superposition model works as the distribution of nucleon interaction points, averaged over many showers, reproduce quite well more realistic calculations accounting for nucleus interactions and break up into remnant nuclei [43]. At present, there is a considerable uncertainty of the predicted shower parameters stemming from our limited knowledge of hadronic multi-particle production. Even if accelerators data exist, their extrapolation to higher energies or phase-space regions of secondary particles needs many model assumptions. Many models exist but still give different result. Nonetheless, at present, they give a correct behaviour and are consistent with existing data as shown in Fig. 12.

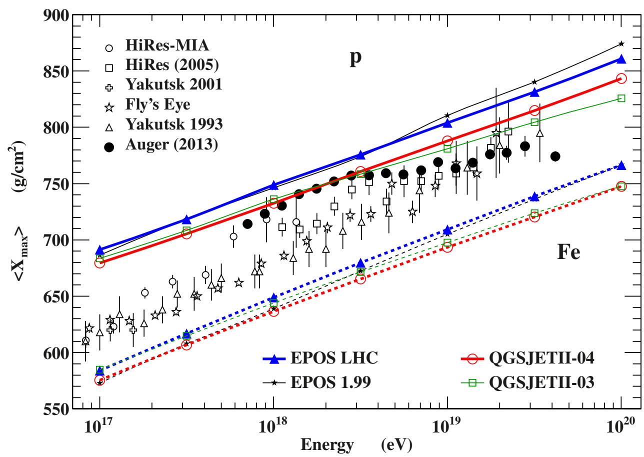

Fig. 12. The $\langle X_{\max}\rangle$ for proton- and iron-induced showers as a function of the primary energy for different high-energy hadronic interaction models overlapping with data. The full lines represent proton and dashed lines iron, with full triangles for EPOS LHC, open squares for QGSJETII-03, open circles for QGSJETII-04 [44].

3. Experimental techniques

The cosmic rays reaching the Earth can be measured directly only outside the atmosphere. This is usually done with satellite experiments, which have the big advantage not to be screened by the atmosphere. At the same time, all the constraints in terms of dimension, power and extreme conditions limit significantly the detector dimension and design. For this, in general, the satellite experiments are suited for the detection of cosmic rays in the energy range of the MeV–GeV. As a matter of fact, at energies higher than that the flux of cosmic rays (particle/square meters/second) is so low that no reasonable statistics can be achieved during the experiment lifetimes, which for satellite is in the order of 5 years.

For this, indirect techniques based on the detection of the atmosphere shower produced by cosmic rays impinging on the atmosphere are mostly used for energies above 100 GeV. The ground based experiment can be divided into two main categories: the Imaging Air-Cherenkov Telescopes (IACT) and the Extensive Air Shower (EAS) arrays. The IACT is a telescope in which the Cherenkov light produced by the charged particles in the shower is collected by a mirror and focussed into a photo-detecting camera. The Cherenkov light can propagate through the atmosphere so, in principle, the telescope can be sitting also at the sea level. In reality, the first interaction happens at tenth of kilometres above the ground, and then the propagation through the atmosphere is attenuated. Therefore, the altitude as an impact of the minimal flux that can be detected, what is directly correlated with the particle energy, as we will show later. As a matter of fact, the highest the energy of the primary, the highest is the flux of Cherenkov photons. At the same time, the rate of cosmic rays decreases with the energy according to a power law. Thus, in general, we can say that for lower energy, we have the fainter Cherenkov light but high flux of cosmic rays, and at high energy, we have stronger light but very low rate. Therefore, the height at which the telescope should be installed need to be chosen according to the energy range of interest. For the EAS detector instead, the technique is to directly detect the charge particles produced in the shower. In general, an EAS experiment is an array composed of different types of detectors to measure the different quantities needed to reconstruct cosmic rays direction and energy. It is clear in this case that the detector has to be near the shower maximum, where the number of particles is maximum and has a not too strong dependence on the shower development. Therefore, the EAS detection requires installations sitting at high altitude. Clearly, the highest is the altitude, the lower is the threshold achievable.

The two approaches are complementary. As a matter of fact, the use of a telescope for the IACT allows to track source with a high precision and then allows also to resolve structure and details of the sources. Pointing precision of fraction of degrees is easily achieved. The energy resolution is also better because, as we will show later, the Cherenkov light flux is proportional to the primary particle energy. With proper calibration, an energy resolution below 10% can be achieved. At the same time, to detect the faint Cherenkov light, the IACT can work only in clear nights and in remote places where light pollution is almost absent. This reduces their duty cycle to less than 10%.

On the contrary, the EAS detectors can work any time and then can reach a 100% duty cycle. At the same time, the reconstruction of the direction and the energy is by far more affected by the event-by-event fluctuation. As a matter of fact, the shower stochasticity is more pronounced with respect to the Cherenkov light production in which the primary energy is completely released into the shower. As a consequence, the measure of many quantities can be done only on a statistical basis but not for each event, and energy reconstruction and calibration are more difficult, and then energy resolution is usually around 20–30%. The reconstruction of the direction also achieves precision of the order of the degree.

All of this will be better discussed in detail for the two key experiments under construction based on these detection techniques, CTA and LHAASO.

The shower development discussed so far is quite general and it is at the basis of the design of calorimeters in collider physics. At the same time, emphasis has been given on processing peculiar atmospheric showers, as the geomagnetic pre-showering and the LPM effects, even though the last ones are in reality also observables in colliders experiments.

It is now necessary to discuss some peculiarities of the atmospheric shower which are important for the two techniques we want to describe.

3.1. Imaging air Cherenkov telescopes

3.1.1. The Cherenkov effect in the atmosphere

Particularly interesting for us is the Cherenkov effect, which is the phenomenon on which the IACT technique is based.

The Cherenkov effect has been known since scientists started to use radioactive materials at the beginning of the XX century. Already Marie Skłodowska-Curie reported on faint blue light glow in highly concentrated radium solutions. Later on, Cherenkov while working with radioactive preparation observed the same blue light glow and started studying it. He found that the light was non-isotropic but correlated with the radioactive distribution and understood this was not a fluorescence phenomenon. The conical wave front of the Cherenkov light had been already predicted by Heaviside in 1888 and by Sommerfeld in 1904, but they were soon forgotten once the speed of light as the universal limit was postulated. Today we know that Cherenkov effect is due to the slower velocity of light in material with respect to the particle velocity itself, while both do not violate the speed-of-light limit. Here, we just recall the fact that this is a threshold effect in the sense that, for it to happen, the particle has to have a velocity greater than the speed of light of the material it is traversing, *i.e.* $\beta_{\rm th} > 1/n$.

This phenomenon can be understood qualitatively by saying that in this condition, the material does not manage to polarise at the speed at which the particle travels. Then the fields in front and the back of the particle are different, and then a sort of some "compensation" is needed not to have a discontinuity of the field in the medium. Then some photons are emitted within a cone around the particle direction with an opening angle $\vartheta_{\rm c}$ such that $\cos\vartheta > 1/\beta c$. As an example, in water $\vartheta_{\rm c} = 42^\circ$, while in neon at 1 ATM it is $\vartheta_{\rm c} = 11$ mrad. The energy loss by the particle due to the Cherenkov emission is below 1% low and then, in general, Cherenkov detectors are used for particle identification. As a matter of fact, particles with different masses accelerated at the same energy having different β can produce or not the Cherenkov light depending if their β satisfy or not the threshold condition $\beta_{\rm th} > 1/n$. Thus, particles with different mass can be identified with the use of the Cherenkov radiator along their path.

The energy lost is converted into photons whose density per unit length ($\mathrm{d}z$) and wavelenght (λ) is expressed by the Franck–Tamm formula

$$\frac{\mathrm{d}^2N_{\rm ph}}{\mathrm{d}z\mathrm{d}\lambda} = 2\pi\alpha Z^2\frac{\sin^2\vartheta_{\rm c}}{\lambda^2} \Longrightarrow \frac{\mathrm{d}^2N_{\rm ph}}{\mathrm{d}X\mathrm{d}\lambda} = 2\pi\alpha Z^2\frac{\sin^2\vartheta_{\rm c}}{\lambda^2}\frac{z_0}{X}\,. \tag{40}$$

The second form in Eq. (40) assumes the so-called "hydrostatic isothermal" atmosphere, in which the atmosphere is assumed as a perfect gas whose density vary with the height z, *i.e.* $\rho(z) = \rho_0\,\mathrm{e}^{-z/z_0}$, where $\rho_0 = 1.2$ kg/m^3.

The quantity $z_0 = RT/gM = 8.4$ km is a constant, where T is the absolute temperature, R the perfect gas constant, M the equivalent molar mass for air and g the gravity acceleration. Then we can say that $\mathrm{d}Z = X\mathrm{d}z/z_0$ and substitute it in the first formula of Eq. (40) to have the second form.

Under the small angle approximation, we have that $\sin^2\vartheta \approx 2(n-1)$. At the same time, under the "hydrostatic isothermal" approximation, the refractive index of air ($n_{\rm air} = 1.000292$) depends only on density of air and then of the pressure. We can then write

$$n - 1 = 2.92\times 10^{-1}\times\frac{P}{T}\frac{288.1\ K^\circ}{P_0} \quad\text{and that}\quad \frac{P}{P_0}\frac{z_0}{X} = \frac{1}{\rho_0}\,. \tag{41}$$

So that we can rewrite Eq. (40) as

$$\frac{\mathrm{d}^2N_{\rm ph}}{\mathrm{d}X\mathrm{d}\lambda} = 2\pi\alpha Z^2\frac{\sin^2\vartheta_{\rm c}}{\lambda^2}\frac{z_0}{X} \approx \frac{4\pi\alpha Z^2}{\rho_0\lambda}\times 2.92\times 10^{-1}\times\frac{288.1\ K^\circ}{T}\,. \tag{42}$$

Remarkably, the Cherenkov yield in Eq. (42), when expressed in the natural variable describing the shower development, does not depend on the local density, *i.e.* it does not depend on the altitude. This means that with the Cherenkov light, a calorimetric measurement is possible even in a deeply inhomogeneous medium like the atmosphere! By integrating Eq. (40) over λ using a typical photosensor wavelength response (350–550 nm), we can calculate how many photons are released

$$\frac{\mathrm{d}^2 N_{\mathrm{ph}}}{\mathrm{d}z} = \int 2\pi\alpha Z^2 \frac{\sin^2\vartheta_{\mathrm{c}}}{\lambda^2} \approx 390 Z^2 \sin^2\vartheta \ \mathrm{ph/cm} = 780(n-1)\ \mathrm{ph/cm}\,, \quad (43)$$

which means few photons per particle per centimetre, but we need to integrate over the particle track length and the number of particles. In our model, each particle travels X_0 before producing a new one, so we can say that the total track length is

$$\begin{aligned} T &= X_0 \sum_{k=0}^{k=t_{\max}-1} 2^k + t_0\, N_{\max}\, X_0 = X_0\left(2^{t_{\max}} - 1\right) + t_0 \frac{E_0}{E_{\mathrm{C}}} X_0 \\ &= X_0\left(2^{\log(E_0/E_{\mathrm{C}})} - 1\right) + t_0 \frac{E_0}{E_{\mathrm{C}}} X_0 \approx (1+t_0)\frac{E_0}{E_{\mathrm{C}}} X_0 \propto E_0\,. \end{aligned} \quad (44)$$

The quantity t_0 represents here the electron range in units of X_0. In air, the electron critical energy is about 100 MeV, and its range varies from about one kilometre at 12 km height down to few hundreds of meters on the ground. The X_0 in air at STP is of the order of hundreds of meters. We can then assume that $t_0 \simeq 1$. In truth, here we are neglecting the fact that only electron contributes, while in reality, electrons and positron are present at each stage. Taking this into account, a more realistic approximation is

$$T = \frac{E_0}{E_{\mathrm{C}}} X_0\, F \quad \text{with} \quad F < 1\,. \quad (45)$$

This means that the total number of Cherenkov photons, which is the integral of Eq. (43) over the total track length in Eq. (44), is proportional to the primary particle energy, which can then be estimated by measuring the photon flux. This is the base of the IACT technique for gamma-ray astronomy, which can then detect showers, measure the direction but also reconstruct the energy of the primary particle measuring the photons flux.

The evolution of the refractive index, due to atmospheric density with the altitude, causes an increase of the Cherenkov angle from about 0.2° at 30 km to less than 1.5° at the sea level. The peculiar fact is that the variation of the Cherenkov opening angle with the altitude compensates the difference in the photon path due to the different height of production. This effect, shown in Fig. 13, is responsible for the formation on the ground of an annulus of about 150 meters centred around the shower axis. As well peculiar is the arrival time distribution of the photons on the ground. In fact, the photons emitted at low altitude, close to the shower axis, reach the detector before those emitted at high altitude. However, the photons emitted at low altitude at large impact distance have a longer geometrical trajectory, which is the sum of track of the charged particle to the emission point plus track of the photon itself. The competition from these two effects compensate almost exactly at a distance of about 120 meters from the shower axis, resulting in a narrow time distribution.

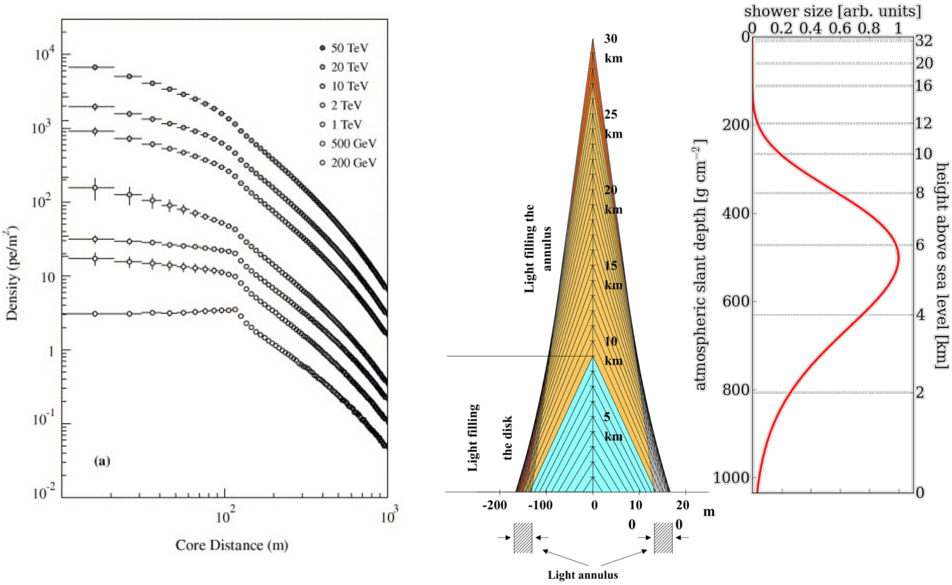

Fig. 13. Air-shower development. On the left, the lateral profile of the photon density for different energies. On the right, the shower development cartoon showing the different light paths of photon produced at different heights and the shower size, *i.e.* the number of particles in the shower as a function of the height.

3.1.2. The gamma-ray astronomy with IACTs

The possibility to detect the Cherenkov light produced by cosmic rays was proved already in 1953 by Galbraith and Jelly using a single PMT and a trash bin (see Fig. 14). They managed to observe signals at a rate of one event every two–three minutes using a trigger threshold of around four times the night sky noise level. By the way, this was the first demonstration that the Cherenkov light was generated also in gases. It took over 35 years before this technique could lead to the first real discovery of a VHE gamma-ray source by the Whipple telescope. This was mainly due to a vicious circle in which scientist were trapped because the poor experiments were giving doubtful results and then funding agencies being sceptical about their potential did not grant funds. In truth, all of this was also due to lack of understanding of the shower fine structure and the limited theoretical knowledge of high-energy hadron interaction, but also due to lack of sophisticated instruments and computing power needed to simulate these

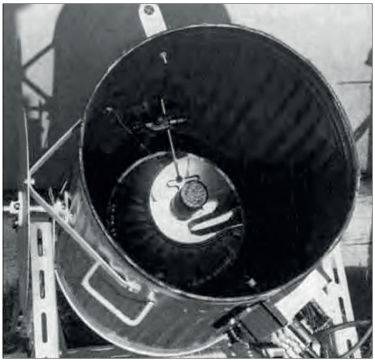

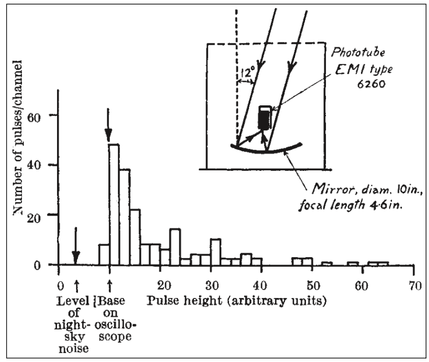

Fig. 14. Left: The Galbraith–Jelly 'telescope' realised by a single PMT (visible in the center) mounted in front of a small mirror mounted inside a trash bin(!) to screen stray light. Right: Result of the measurement obtained with a threshold 5 times higher than the Night Sky Background [45].

processes. In 1989, the Whipple Collaboration published the first convincing observation of gamma-ray emission from the Crab nebula, using the 10-m diameter telescope at the Fred Lawrence Whipple Observatory in Arizona, USA. The telescope was built in 1968 but could not manage to find gamma source until Trevor Weekes and his team found the right keys to open the door to gamma-ray astronomy. This success is the combination of 3 main factors, which set the basis of the next IACT instruments. The first one is a natural ingredient of many projects: good luck! As a matter of fact, the Whipple Collaboration focused their studies on the Crab nebula, which turned out to be the strongest steady-state galactic gamma-ray source and, in fact, it is at the moment used as a standard candle and unit of measure to assess telescopes sensitivity. The second is the use of a large light collection area (mirror dish) but mostly the adoption of an imaging camera, which was the key to achieve a gamma/hadron separations. As a matter of fact, the difference in the physics of the shower between gamma and hadron (see the top row of Fig. 15), produces quite different images on an imaging camera (bottom row of Fig. 15), and then a more effective gamma/hadron separation can be achieved. The third factor was the introduction of a refined gamma/hadron separation method based on the calculation of image moments, *i.e.* an analysis based on the combination of both a measurement of the shower image orientation and an analysis to evaluate the difference in images between gamma-ray showers and hadron showers. In truth, all of this was possible and was successful mostly for the use of simulations which provided an invaluable help to define the design and the analysis strategy. This experiment was the basis of the gamma-ray astronomy and also showed that simulations are a key point for the success of this science.

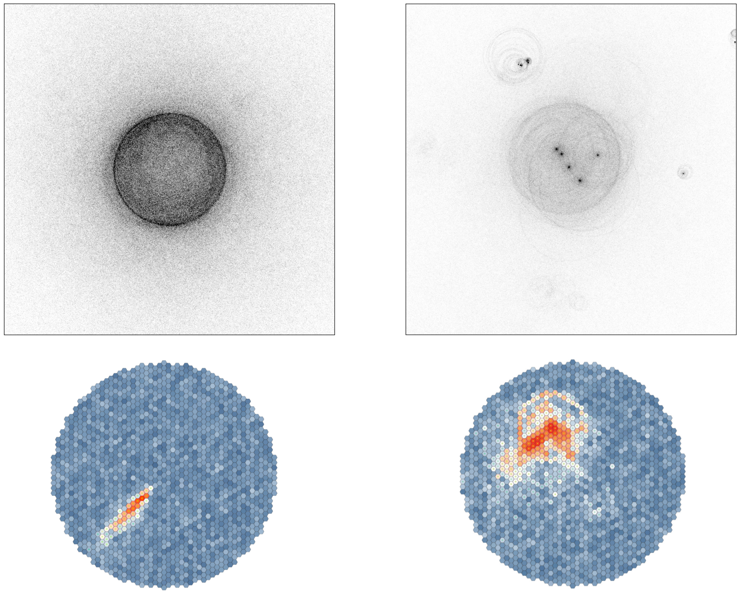

Fig. 15. Top row: Image of shower light pool on the ground from simulation, for shower from gamma (left) and hadron (right) with the same energy. Bottom row: Simulation of shower image as reconstructed with an imaging Cherenkov camera.

3.1.3. The Cherenkov Telescope Array (CTA)

The Cherenkov Telescope Array (CTA) is an international initiative to build a next generation instrument for detecting the gamma ray with a sensitivity at least ten times better than current instruments in a wide energy range from tens of GeV up to 300 TeV. CTA will be operated as an open observatory aiming at covering the full sky. To achieve such a scope, CTA will consist of two arrays, one located at Canary island of la Palma in the Observatory of Roches de los Muchachos, covering the northern sky, and one in the Paranal desert in Chile in the nearby of the European Southern Observatory, covering the southern sky. The site in the southern hemisphere is conceived to study the wealth of sources in the central region of our Galaxy and the richness of their morphological features. The northern site complements the southern one, and it will be primarily devoted to the study of Active Galactic Nuclei (AGN) and cosmological galaxy, and star formation and evolution.

The IACT telescope design can start from few simple considerations. As shown before, the photon flux is proportional to the particle energy. The number of photons measured by the camera depends on the shower flux but also on the collection area and the light detector characteristics.

CTA design is based on well identified design drivers, which shape the layout, the types of telescopes and the technologies used. As mentioned before, CTA aims at providing a uniform energy coverage for photons from several tens of GeV to beyond 100 TeV with a sensitivity increase of an order of magnitude with respect to current instruments and increased angular resolution to have the ability to resolve the morphology of extended sources [46]. In fact, in order to increase the statistics of the astrophysical object, particularly important for transient phenomena and to cover highest energies, CTA wants to boost significantly the detection area and hence detection rates and enhance the sky survey capability, monitoring capability and flexibility of operation. The last one is a key feature for CTA aiming at being operated as a proposal-driven open observatory, with a Science Data Centre providing transparent access to data, analysis tools and user training.

As shown before, there is a direct connection between the energy and the photon flux (see Fig. 16 (left)). If a Cherenkov camera needs a minimal flux of photons to trigger an event, then the minimal energy, *i.e.* the energy threshold, depends on the mirror size. As a matter of fact, a larger mirror, *i.e.* collection area focussing on the small area of a camera, allows to detect fainter shower.

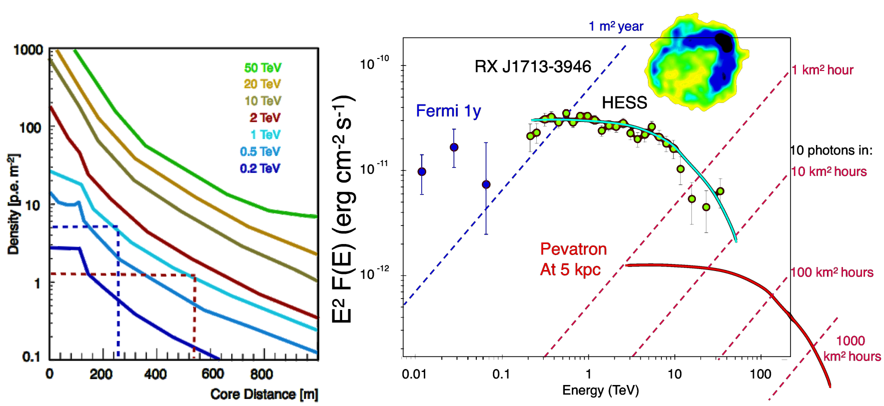

Fig. 16. Density of photons as a function of the distance from shower axis for different energies (left). Flux of gamma ray as a function of the primary energy. On the right are also drawn some dashed lines which give the time needed and the surface to the instrument to be able to collect 10 photons.

At increasing energy, the photon flux increases, and then small mirror is sufficient to detect showers, but at the same time the gamma-ray flux decreases with an exponential law which means that the number of showers per second and unit area becomes small. As an example, from Fig. 16 (right), it can be seen that at 3 TeV to collect 10 photons it is needed to instrument an area of 10 km^2 and wait for 1 hour, or respectively wait 10 hours on a surface of 1 km^2. It is then evident that for low energy, where the cosmic ray rate is high, but showers are fainter, it is needed a telescope with a very large area. On the contrary, at high energy, the cosmic ray rate per area is quite small and then a large area needs to be instrumented. At the same time at high energy, a small mirror is enough to trigger showers even if they are distant hundreds of meters away (see Fig. 16 (left)). From this consideration, it descends immediately that a single telescope type cannot accommodate the wide energy range targeted by CTA.

CTA array is composed of three different types of telescopes. The Large Size Telescope (LST), with a mirror dish of 23 meters in diameter, targets energies greater than 30 GeV. Its sensitivity is optimised for energies from 30 GeV up to 1 TeV above which other types of telescopes dominate the sensitivity. The Medium Size Telescopes (MST), with a mirror of 12 meters in diameter, dominate the sensitivity between 300 GeV and 30 TeV, while the Small Size telescopes (SST) with a mirror dish of 4 meters in diameter, dominates sensitivity for energies above few TeV. The number of telescopes depends on the energy range they target and clearly increases with energy. This is related to the event rate per area which decreases with a power law when energy increase. At the same time, the spacing is also relevant for the triggering and for energy and angular resolution. If, in fact, a shower is detected by more than one telescope, its energy and direction can be more precisely reconstructed. In order to identify the right trade-off between number of telescopes and cost/over performance ratio, Monte Carlo can be used to optimise the layout and the distance between telescope. In the case of CTA, many different layouts have been simulated and the one chosen is shown in Fig. 17.

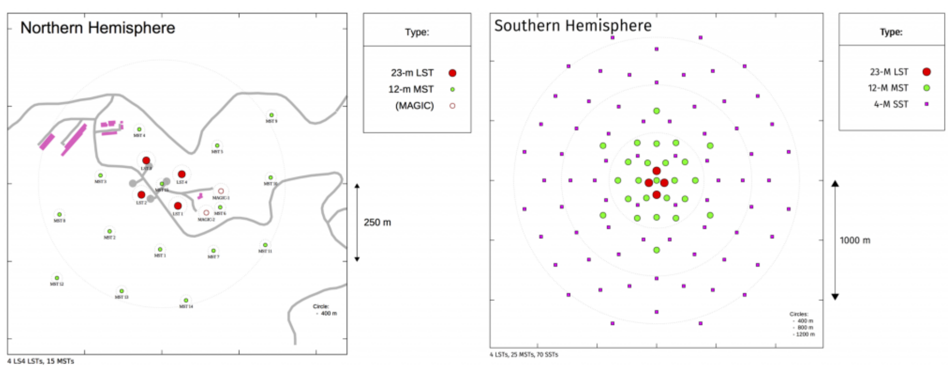

Fig. 17. CTA arrays layout. The northern site (left) will be composed of 4 LSTs and 15 MSTs to cover an area with a radius of about 250 m. The southern site will be composed of 4 LSTs, 25 MSTs and 70 SSTs covering an area with a radius of about 1 km.

The sensitivity reported in Fig. 18 corresponds to the layout of two arrays as shown in Fig. 17, where the different number of telescopes at the northern site (left) and the southern one (right) is visible. This is reflected in the lower sensitivity at energy above one TeV for the northern site, which has a smaller area and where the SSTs are missing.

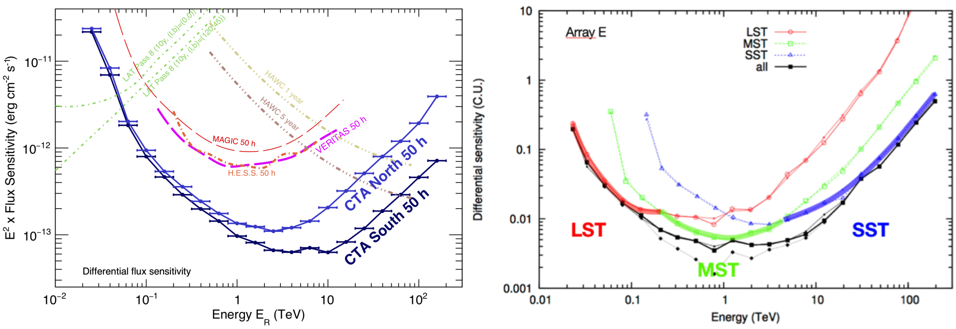

Fig. 18. Left: The official CTA differential sensitivity as a function of the energy for the final layout. Right: An old study to illustrate how the different telescope types contribute to the overall sensitivity.

One of the design goals, the ability to resolve the morphology of extended sources, depends on the angular resolution. The limiting factors for the angular resolution are the pointing precision and the Point Spread Function (PSF). By pointing precision, we refer to the capability to know with a high accuracy the absolute position of the telescope's optical axis which is the reference to trace the shower direction. This is the convolution of many factors. The telescope's structure under the effect of the gravity and the wind undergos small elastic deformation which can cause an apparent shift of the source position. This effect can be measured and modelled to produce a bending model which can be used either to correct the telescope position on-line, or in the off-line analysis to recover the absolute position of the source. This usually done by means of optical camera mounted on the mirror dish pointing at the sky and having in its field of view both the Cherenkov camera and the stars behind it. In this way, analysing the images is possible to reconstruct the position of the telescope optical axis and of the Cherenkov camera with respect to known stars. This kind of measurement are so precise that can also spot rotation or tilting of few millimetre of the foundation of the telescope due to the soil viscosity changes for the effect of the rain! In truth, the ultimate precision is limited by the camera pixel size and the PSF. The PSF is a parameter which describes the optical quality of the telescopes. It is the measure of the spot size on the camera plane corresponding to a star, which is well approximating a point source at infinity. The star is a point source which is blurred in a spot when focussed by the mirror having a fixed focus. The size of the spot depends on the mirror quality but is also limited by the fact that an optical system has always an optimal working range and cannot accommodate any image at any distance. The simplest optics for this type of telescopes is the Davies–Cotton, in which the mirror is composed of identical facets, all having the same radius of curvature which defines together with the dish mirror diameter also the distance at which the camera has to be put. The parameter f/D is the ratio between the dish diameter D and the focal length f, *i.e.* the distance at which the mirror focusses the light. Usually, the mirrors have a radius of curvature which is twice the focal length. As an example for an $f/D = 1.4$ for a mirror of 4 meters, the focal point, where the camera should stay, is at 5.6 m and the mirror radius of curvature is 11.2 m. The mirror facet roughness and surface precision, *i.e.* how much it reproduces the spherical surface, contribute to the PSF. For a mirror composed of many facets all focussing in the center of the camera, the total PSF is the convolution of the PSF of the single mirrors and it greatly dependent on the precision in aligning the different facet at the same point. The mirror alignment is, in fact, an important part of the commissioning and it is usually repeated over time. As a matter of fact the facets are connected with the structure with some support which can be moved to correctly align them. This is done with some actuators which can be either manual or automatic. The simple concept of actuator is a screw, which can push on the mirror and displaced it when held by a fixed point. Usually with a fix point holding the facets and two actuators is possible to move the facets focussing point all over the camera plane. The actuator, at the same time, cannot be completely rigid, or it can happen that an external event can displace the mirror facets and spoil the alignment. That is why the alignment is monitored over time and redone regularly. The things are not that easy, as the response of the telescope off-axis also distort the shape of a point source. In the case of the Davies–Cotton design for example, the PSF degrade quite rapidly at few degrees from the optical axis. For a good understanding of the Cherenkov optics see Ref. [47]. The PSF of CTA is shown in Fig. 19 compared with the one of the High Energy Stereoscopic System (HESS) an IACT array composed of 4 small telescopes and a large one. In the same figure, there is also reported the extension corresponding to 1 arc-minute. CTA aims at having an angular resolution of less than 10 arc-second, which would allow to do morphological studies of the sources with an unprecedented precision in the gamma-ray domains. The PSF is also important for the camera angular pixel size. Clearly smaller pixels mean a more resolved image, but then a larger number of pixels is needed to instrument the same area, increasing cost and complexity of the camera. Therefore, the pixels size has to be small enough to have well-resolved images, but at the same time, cannot be smaller than the PSF, otherwise the resolution would be washed out by the optics. In general, the pixels have to be small but yet comparable with the PSF. Another important feature is the Field-of-View (FoV). CTA aims at having a large FoV to be

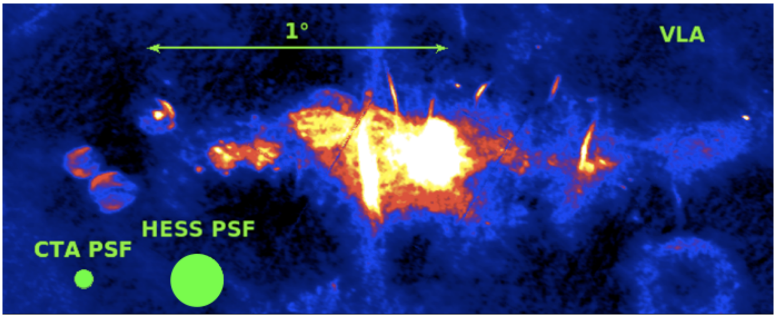

Fig. 19. The Cygnus pulsar as seen by the Very Large Array (VLA) in the radio domain compared with the PSF of CTA and HESS, one of the current IACT array. The angular extension of 1 arc-minute is also shown.

able to survey large zone with a single observation. This is not trivial as the FoV is directly related to the camera instrumented area. This means that covering a larger area requires a larger number of pixels. The number of pixels is clearly not only limited by the cost, but also but the complexity, power consumption, cooling capacity, weight *etc.* That is why also in CTA the number of pixels is below 2000 for any of the different cameras. Given the different optics, the pixel size is different and then even if the number of pixels is the same, the FoV of the telescopes is different. In the case of CTA, while the LST and MST have a FoV around 4.5°, for the SST can go beyond 9°. With its larger FoV, high sensitivity, higher resolution and wide energy range, CTA can perform a survey of the galactic center in a time

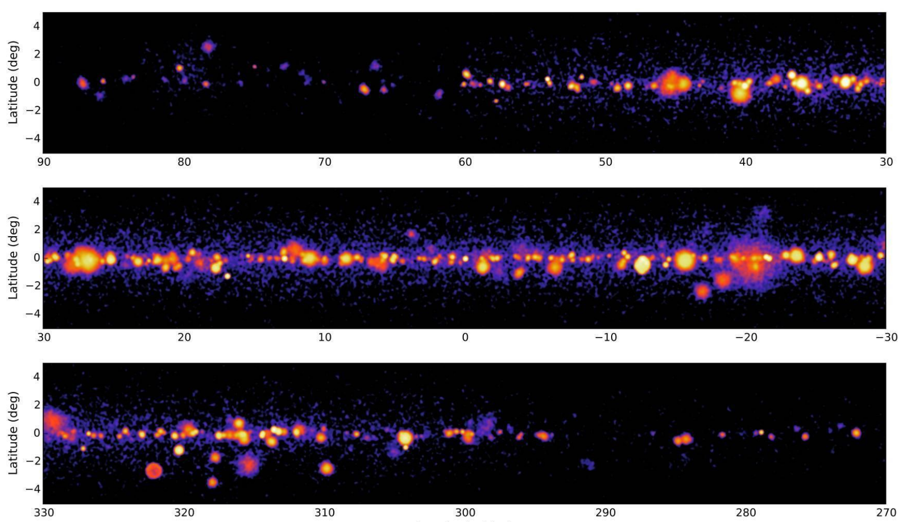

Fig. 20. Simulation of the Galactic Center Survey as can be done by CTA.

which is two order of magnitude shorter than current instruments as HESS, with a higher accuracy and more resolved images. In Fig. 20, the simulation of how a survey of the achievable galactic plane would look like is shown.

A detailed and complete overview of the CTA science can be found in a recent science book [48], where all physics topics are extensively discussed.

3.2. The extended air-shower arrays

The EAS experiments, in general, target at the measurement of cosmic rays at wide and do not restrict themselves to gamma-ray astronomy only. They, in fact, try also to cover a higher energy range to measure the knee region above which CRs composition studies are possible. At that energies, as we have already shown, the event rate is quite small and large instrumented area are needed.

During the development of air shower different types of particle are produced (see Fig. 21).

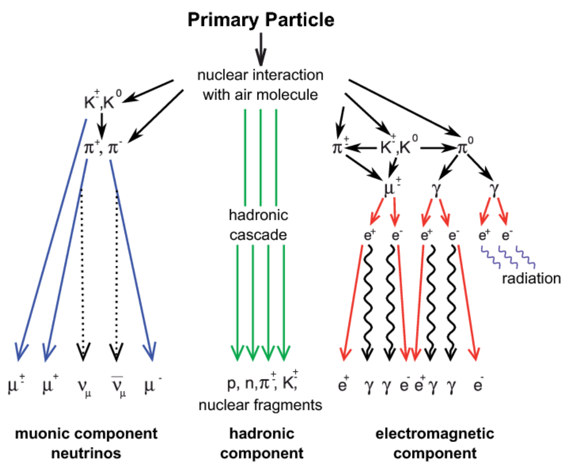

Fig. 21. Schematic of an EAS highlighting all different components.

It is evident that the different particles have different energies and type of interaction and that is why surface arrays usually are composed of different type of detectors.

The most used technique is based on detection of the Cherenkov light. A large volume of water is used as a target for charged particles which produce the Cherenkov light when traversing it. In general, a single PMT is enough to detect the light and its intensity which is proportional to the charged particles density, which in turn is proportional to the energy of the primary. This technique, for example, is used in the HAWC array, where 300 tanks, 5 meters high and with a diameter of 7.3 meters, instrument an area of 22,000 square meters. It can detect a shower with an energy ranging from 100 GeV up to PeV.

It is clear that the number of particles depend on the stage of the development of the shower and then energy reconstruction is much less precise than in the case of IACT, where the light is detected far away from the end of the shower, and then the energy is completely released and the measurement is calorimetric.

3.2.1. Fluorescence

The electron in the shower can excite the nitrogen molecule of the atmosphere which de-excite through the emission of fluorescence photons.

The emission is mostly due to the level $2P$ of molecular nitrogen N_2 or the $1N$ of the molecular nitrogen ion N_2^+ whose corresponding spectrum is shown in Fig. 22. The emission is mildly altitude- and temperature-dependent. The

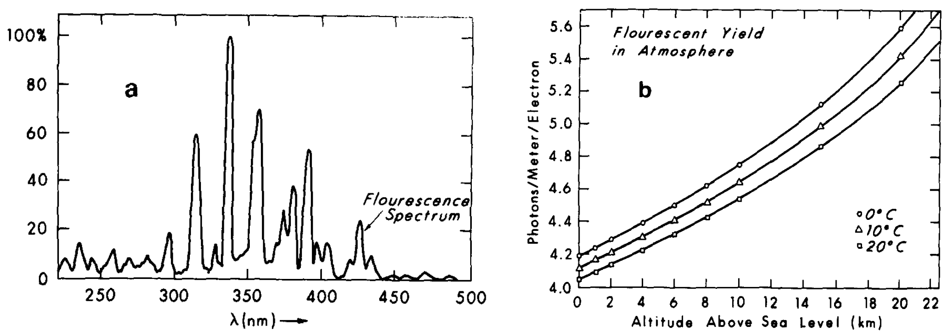

Fig. 22. Atmospheric fluorescence spectrum due to nitrogen (a) and fluorescent yield (equivalent 360 nm photons/electron/m) (b) as a function of altitude (km) measured at Utah Eye Fly [49].

altitude dependency is a fortuitous result of two competing effects. While the number of molecules excited per unit path length grows proportionally with pressure, the probability of fluorescence emission decreases as it increases the probability of de-excitation by collision. For the ground base experiment, located below 5 km, a good approximation for the yield is 4 photons/m per electron. In any case, the fluorescence light yield depends on many factors so, in general, every experiment tries to estimate it comparing data with Monte Carlo simulations. The fluorescence emission is almost isotropic and its angular distribution can roughly be approximated by $\mathrm{d}N/\mathrm{d}\Omega \approx N_\gamma N_e/4\pi$, where N_γ is the fluorescent yield in photons/electron/m and N_e is the number of electrons in the shower. The resultant light yield corresponds to a scintillation efficiency of only 0.5%. It is evident that this light is much fainter than the Cherenkov light and then the fluorescence can be used only for shower far away, and then outside the Cherenkov light cone. In this case also the light emitted depends on the track length that we have shown to be proportional to energy and then also the fluorescence allows for a calorimetric measurement.

However, the poor efficiency is compensated for by the huge amount of energy released by the shower, *i.e.* the number of electrons, which for a 100 EeV proton is greater than 1 J in 30 μs. For event with energy above the PeV, the shower can be detected from 10 kilometres.

The detection of showers via fluorescence has been successfully exploited by many experiments, both on balloon [49] and on ground [50, 51].

3.2.2. EAS lateral shape

To have a good estimation of the shower energy, it is then important to estimate also the shower development stage, also called the shower age. For the EM component of the shower, we know that the lateral profile scales with the Moliére radius R_{M}, which, under approximation of hydrostatic atmosphere, varies inversely with the medium density as [52]

$$R_{\mathrm{M}}(h_0)\frac{\rho_{\mathrm{atm}}(h_0)}{\rho_{\mathrm{atm}}(h)} \approx \frac{9.6\ \mathrm{g\,cm^{-2}}}{\rho_{\mathrm{air}}(h)}\,. \tag{46}$$

The lateral shower profile, or better its Lateral Distribution Function (LDF), in three dimensions has been approximately calculated by Nishimura and Kamata [53], and later improved by Greisen [54] (NKG)

$$\rho_{\mathrm{ch}}(r) = \frac{N_{\mathrm{ch}}}{2\pi R_0^2}\, C \left(\frac{r}{r_0}\right)^{s-2} \left(1+\frac{r}{r_0}\right)^{s-4.5}\,, \tag{47}$$

where the constant is

$$C = \frac{\mathit{\Gamma}(4.5-s)}{2\pi \mathit{\Gamma}(s)\mathit{\Gamma}(4.5-2s)}\,. \tag{48}$$

The parameter s is the shower age, which substantially gives an indication of the stage of the development of the shower. For any atmospheric depth, $0 < s < 3$, and $s = 1$ at shower maximum. It is defined as

$$s = \frac{3t}{t+2t_{\max}}\,, \quad \text{where} \quad t = \frac{X}{X_0} = \int_z^\infty \rho_{\mathrm{atm}}(z)\frac{\mathrm{d}z}{X_0} \tag{49}$$

and $t_{\max} = \ln(E_0/E_{\mathrm{C}})$. If integrated over the shower footprint for an EM shower, the formula gives also the number of particles as

$$\bar{N}_e(t) = \frac{0.31}{\sqrt{t_{\max}}}\,\mathrm{e}^{\left[1-\frac{3}{2}\ln(s)\right]t} \xrightarrow{s=1} \frac{0.31}{\sqrt{t_{\max}}}\,\frac{E_0}{E_{\mathrm{C}}}\,. \tag{50}$$

For a 30 GeV photon at $s = 1$, $N_e \simeq 50$, while at 1 PeV, it becomes $N_e \simeq 9 \times 10^5$.

Finding the relation between the ground parameter and primary energy has to deal with two main problems. One is the modelling of the shower development coming from the indeterminacy still existing in hadronic interactions, which is not entirely determined by accelerator experiments. The other problem arises from the large fluctuations in the particle density on ground $N_{\rm g}$ for a fixed E_0 and *vice versa* due to both different kinds of primary nuclei likely to be present and from fluctuations in the shower development.

As a result of the fluctuations of the observed number of particles $N_{\rm g}$ for fixed E_0 (see Fig. 23) in the presence of a steep spectrum, the ratio of mean energy for showers of the same observed size, $\langle E_0\rangle/N_{\rm g}$, is smaller than the ratio $E_0/\langle N_{\rm g}\rangle$, where $\langle N_{\rm g}\rangle$ is the mean ground parameter of a sample of showers all of which have the same energy.

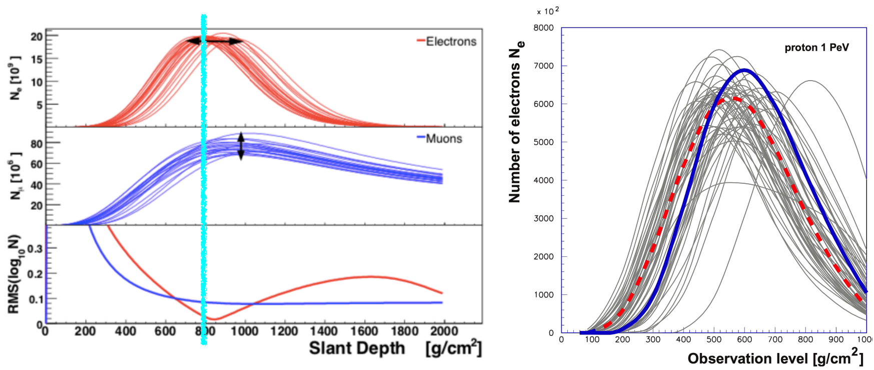

Fig. 23. (Colour on-line) Left: Fluctuation of longitudinal profile for electrons and muons (two upper panels) and the RMS of the fluctuations (bottom panel). Right: There is shown the measured number of electrons on ground for 1 PeV protons. Solid/blue line shows the profile corresponding to $N_e = \langle N_e\rangle$, while dashed/red line shows $X_{\rm max} = \langle X_{\rm max}\rangle$.

LDFs are generally of phenomenological nature, as they need to specifically adapt to the particular detector array under consideration, since they have different detection thresholds, detector response and observation level. In general, they are not comparable with each other and, as a matter of fact, a certain "zoology" exist

$$\rho_{\rm ch}(r) = \frac{N_{\rm ch}}{2\pi R_0^2} C_1 \left(\frac{r}{r_0}\right)^{s-2} \left(1+\frac{r}{r_0}\right)^{s-4.5} \left(1 + C_2\left[\frac{r}{r_0}\right]^d\right), \qquad (51)$$

where $C_2 = 1/11.4$ and $C_1 = [B(s, 4.5-2s) + C_2 B(s+d, 4.5-d-2s)]^{-1}$ and B are the Euler functions. For showers of the size of $N_e \approx 10^6$ at the sea level, Greisen [54] uses $s = 1.25$, $d = 1$ and $C_2 = 0.088$, while Nagano [55] at 920 g/cm^2 uses $d = 1.3$ $C_2 = 0.2$ and s fitted for each shower.

The AKENO experiment adapted the Greisen formula to better describe the large showers it detects and for which the analytical integration from 0 to infinity cannot be given

$$\rho_{\mathrm{ch}}(r) = \frac{N_{\mathrm{ch}}}{2\pi R_0^2}\, C_3 \left(\frac{r}{r_0}\right)^{s-2} \left(1+\frac{r}{r_0}\right)^{s-4.5} \left(1+\beta\frac{r}{r_0}\right)^{\nu} . \tag{52}$$

The AGASA experiment, to describe the LDF up to a distance of several kilometres from the axis for EeV showers, uses yet another formulation

$$\rho_{\mathrm{ch}}(r) = C \left(\frac{r}{R_{\mathrm{M}}}\right)^{1.2} \left(1+\frac{r}{R_{\mathrm{M}}}\right)^{-(\eta-1.2)} \left(1.0+\left(\frac{r}{1\ \mathrm{km}}\right)^2\right)^{\delta} , \tag{53}$$

where the parameters are $\eta = 3.8$, $\delta = 0.6 \pm 0.1$ and a Molière radius $R_{\mathrm{M}} = 91.6$ m for near vertical showers with $\sec(\vartheta) < 1.2$.

To represents the lateral signal density $S(r)$ produced by charged particle in water Cherenkov detectors, the Haverah Park experiment uses

$$S(r) = \begin{cases} k\, r^{-\left(\eta+\frac{r}{r_0}\right)} & r < 800\ \mathrm{m} \\ \left(\frac{1}{800}\right)^{\beta}\, k\, r^{-\left(\eta+\frac{r}{r_0}\right)+\beta} & r > 800\ \mathrm{m} \end{cases} \tag{54}$$

with $r_0 = 4000$ m, and the zenith-dependent shape parameter η, which has some mass dependence sensitivity for shower above 3×10^{17} eV.

The Pierre Auger experiment instead uses a modified NKG of the form of

$$S(r) = C \left(\frac{r}{R_{\mathrm{M}}}\right)^{-\alpha} \left(1+\frac{r}{R_{\mathrm{M}}}\right)^{-(\eta-\alpha)} , \tag{55}$$

where R_{M} is the Molière radius, C is proportional to the shower size, while η and α are parameters determined experimentally.

In truth, there are many other more or less complex functions to describe LDF depending on the type of detectors which compose the array. The integrated LDF, which represents the total number of charged particle in a shower, is related to the primary energy. Unfortunately, such a relation depends on the type of the primary and it impacts the measurement of spectra in the knee region, which differs among the different experiments and whose discrepancies are difficult to reconcile. As a matter of fact, not only the knee positions, but also the shapes of the spectra differ according to different observation levels, zenith distances, and different particle detection thresholds, but also for the different detector response functions and calibration methods.

The muon components can also be used to improve the shower reconstruction especially for array which can detect it independently, as LHAASO. In this case, the total number of muons, together with their lateral distribution and arrival time, can be used. In analogy with what was done for charged particle, the lateral muon density distribution can be sampled, and the total muon number can be determined. On the contrary, a standard lateral distribution functional form for muon density does not exist.

Compared to the EM case, the muons in the shower are certainly more broadly distributed and their number does not decrease rapidly with the shower age. In addition, the unknown properties of hadronic interactions at the highest energies affect the longitudinal development, inducing some model dependence also in the expected lateral distribution Experimental effects such as muon detectors energy threshold as well as the distance from the point of maximum muon production to the core at the ground level, also affects the shape of the lateral distribution.

One parametrisation has been suggested by Greisen [54]

$$\rho_\mu(r, N_\mu) = C N_\mu \left(\frac{r}{r_{\mathrm{G}}}\right)^{-\beta} \left(1 + \frac{r}{r_{\mathrm{G}}}\right)^{-2.5}, \tag{56}$$

where $r_{\mathrm{G}} = 320$ m is the Greisen radius. A quite general form of the formula used by many experiment is [56, 57]

$$\rho_\mu(r) = K\, r^{-\alpha} \mathrm{e}^{-\frac{r}{r_0}}, \tag{57}$$

where K, α and r_0 are parameters to be fitted on data.

The lateral distribution functional forms discussed so far are assumed azimuthally symmetric and, as such, pertain to the perpendicular distance from the shower axis. In real life, showers are however inclined to have the density on the ground not azimuthally symmetric to the core location. As a consequence, the distance from the core along the ground is different with respect to the perpendicular distance to the shower axis. In addition, the shower age at the ground level differs for different azimuths, and geomagnetic effects on charged particle disrupt azimuthal symmetry.

In the shower models shown so far, the effect of the atmosphere can be accounted as a function of the slant depth t. Under this assumption, the LDF for any zenith angle lower than 70° can be rescaled to the vertical case by defining an equivalent slant depth t' according to

$$t'(\vartheta, \zeta) = t \sec\vartheta (1 + K \cos\zeta)^{-1}, \tag{58}$$

where ζ is the azimuthal angle in the shower plane, $K = K_0 \tan\vartheta$ and K_0 is obtained by fitting [52].

For zenith angles greater than 70°, the electromagnetic component at ground is mainly due to muon decay, though hadronic interactions still also contribute, pair-production and bremsstrahlung, even if to a much smaller extent. As a result, the lateral distribution follows that of the muon rather closely.

For vertical showers, the ratio of electrons to muons depends strongly on the distance from the core. As an example, for a 10^{11} GeV vertical proton shower, it varies from 17 to 1 at 200 m away from the core to 1 to 1 at 2000 m. For inclined showers, the ratio behaves somewhat differently, for zenith angles greater than 60°, the ratio stays roughly constant at a given distance from the core. The ratio decreases when the zenith angle exceeding 60°, until at 75°, it becomes 400 times smaller than for a vertical shower. At the ground, also the average muon energy changes dramatically for inclined shower. For vertical showers, the average muon energy is 1 GeV, while for horizontal showers, it can be about 2 orders of magnitude greater. This is due to a combination of energy loss mechanisms and the finite muon lifetime which filtered out muons of lower energy.

3.2.3. Longitudinal profile

The longitudinal development of the shower is the result of the development of the three components highlighted in Fig. 21. The backbone of an air shower is the hadronic component (mostly pions), which also feeds the electromagnetic and muonic components. While the electromagnetic component has the typical growth, reaching a maximum and then decaying once the critical energy is reached, the muon components having reached the maximum, decay quite slowly as the muons are MIP and then very penetrating. For the electron component, one of the most used parametrisation is the one by Gaisser–Hillas [58]

$$N_e(X) = N_e^{\max}\, \mathrm{e}^{\dfrac{(X_{\max}-X_0)}{\lambda}} \left(\frac{X-X_0}{X_{\max}-X_0}\right)^{\dfrac{(X_{\max}-X_0)}{\lambda}}, \qquad (59)$$

where X is the depth at observational level, X_0 the depth of the first interaction, $X_{\max}$ the depth of the shower maximum and λ the interaction length, which is around 70 $\mathrm{g\,cm^{-2}}$. Using the Gaisser–Hillas parametrisation in Eq. (59), fluorescence detectors can measure $X_{\max}$ with a statistical precision of about 30 $\mathrm{g/cm^2}$.

The quantity $X_{\max}$, and then also the difference $(X_{\max} - X_0)$, depends on primary energy E_0, while the difference $(X - X_0)$ is an indication of the shower stage, which increases approximately logarithmically with E_0. Therefore, with such a parametrisation, it is possible to extract the $X_{\max}$ for each shower and estimate the energy on a statistical basis with an energy calibration.

A more general form of Eq. (59) is obtained with the following parametrisation:

$$F(X) = F_{\max} \left(\frac{\xi}{\eta}\right)^{\eta} \mathrm{e}^{\eta-\xi}\,, \tag{60}$$

where $\xi \equiv (X_{\max} - X_0)/\lambda$ is the shower *depth* measured in unit of λ, relatively to a reference depth X_0, which is not the radiation length, and $\eta \equiv (X - X_0)/\lambda$ is the profile *width* measured in unit of λ as well.

The set of parameters $(F_{\max}, X_{\max}, X_0, \lambda)$ is used to fit the longitudinal profile. When there is not enough data to constrain the fit, it is usually fixed $\lambda = 70\ \mathrm{g\,cm^{-2}}$ and performed a three parameters fit. For shower measured only around $X_{\max}$, usually λ and $X_0 = 0$ are fixed, while $F_{\max}$ and $X_{\max}$ are fitted. It is worth to note that the parameter X_0 should not be interpreted as the first interaction depth. As a matter of fact, longitudinal profiles fitted with Monte Carlo, as QGSJET and SYBILL, as well with real data are best fitted with negative values of X_0.

The longitudinal profile of a shower usually refers to the number of charged particles N_e, and in this case, $F_{\max}$ corresponds to the shower size at maximum $N_{\max}$. In the case of the fluorescence light, the measurement as a function of depth relates more closely to the energy deposition rate $\mathrm{d}E/\mathrm{d}X$, and the integral of the functions gives directly the total energy deposited in the atmosphere. In this case, the *longitudinal profile* pertains more the energy deposition rate, *i.e.* $F \equiv \mathrm{d}E/\mathrm{d}X$, than the energy deposited. The integral of the function in Eq. (60) has a closed form in terms of the standard Gamma function

$$\begin{aligned}
&\int_0^\infty F_{\max} \left(\frac{\xi}{\eta}\right)^{\eta} \mathrm{e}^{\eta-\xi} \lambda\ \mathrm{d}\xi \\
&= F_{\max}\, \lambda \left(\frac{e}{\eta}\right)^{\eta} \int_0^\infty \xi^{\eta} \mathrm{e}^{-\xi} \mathrm{d}\xi \\
&= F_{\max}\, \lambda \left(\frac{\xi}{\eta}\right)^{\xi} \Gamma(\eta+1)\,.
\end{aligned} \tag{61}$$

Finally, if $F(X)$ is $\mathrm{d}E/\mathrm{d}X$, then the integral in Eq. (61) represents the total electromagnetic shower energy. Instead, if $F(X)$ is the number of charged particles $N_e(X)$, then the integral gives the electromagnetic shower energy, once it is multiplied by $2.2\ \mathrm{MeV/g/cm^2}$, which is the typical energy deposition per charged particle (see Sec. 2.1).

An essential feature for discriminating the mass of the primary is shift of $X_{\max}$ with the primary nucleus mass A proportional to $\ln(A)$.

The dependence of $X_{\max}$ with energy, known as the elongation theorem, showed in Eq. (35), for a purely EM shower gives $\Lambda = X_0$. For hadronic showers, instead, the dependence is more complex, and it has been shown that assuming the superposition model, it can be written as [59]

$$\Lambda = X_0(1 - B)\left[1 - \frac{\langle \ln A \rangle}{\ln E}\right] . \tag{62}$$

As an example, the shift between iron and proton ($X^{p}_{\max} - X^{Fe}_{\max}$) is about 100 $\mathrm{g\,cm^{-2}}$.

Moreover, the muon content of the shower depends on the energy of the primary. Heavy nuclei have a higher muon content with respect to light ones or proton (see Eq. (39)). The exact ratio depends on the model of hadronic interaction used. Qualitatively, this can be understood by recalling that muons are produced by pions, so they start being produced at the shower stage where pions decay. Given the superposition model for a heavy nucleus, this energy threshold is reached at earlier stages as the initial energy is shared by the nucleons.

Of course, the muon fraction depends on many other factors such as the longitudinal and transverse position, which make it to increase with X and with the distance from the core. For the variation of the density and the dependence on the direction angle ϑ at large zenith angle, also the hadronic cascade develops at a higher altitude, the pions decay earlier (in terms of the slant depth) giving less muons, with a larger mean energy, *i.e.* carrying globally a larger fraction of E_0.

The muon components play also a major role in the gamma/hadron separation. In fact, the gamma-ray shower has few muons in the core, while the hadron shower has many more muons, also with higher transverse momentum coming from the pion decays.

As we will show later, this is used in LHAASO to achieve a very good discrimination by measuring the EM components and the muons independently.

3.2.4. Reconstruction of shower parameters

Shower direction

The determination of the shower direction (axis) and the core location are mandatory steps to identify sources, but as it has been shown before, they are also needed to improve the shower profile fit.

A pure "geometrical" reconstruction is the simplest approach and it is usually also the first step for fitting procedures. If three detectors of the array detect a shower by knowing their position, the shower direction can be reconstructed finding the unique speed-of-light downwards shower front that can accommodate all three signals. Clearly, the more stations record the shower, the more precise the shower front can be reconstructed using a least square method. The time resolution of detectors plays then a fundamental role in an accurate reconstruction. For the determination of the shower axis position, the circular symmetry of the particles density around shower axis is exploited. For shower along the vertical, the symmetry on the ground is circular and becomes elliptical as soon as the axis moves away from the zenith. An initial estimate of the shower core can be obtained using the centre-of-gravity of the density measurements. By using these estimations, core estimates and the shower axis, the most probable core position and size can be reconstructed by fitting the LDF.

Once the core has been re-evaluated, it is possible to re-fit the timing shower front profile taking into account its curvature. There are some subtleties to take into account, for example, the sparseness of typical surface arrays as well the sparseness of the particles in the shower front itself, especially far from the core. This requires a careful definition of what is meant by the shower-front arrival time at a detector plane, and a proper representation of the fluctuations expected because of the sparse sampling. LHAASO in this sense will improve significantly the detector sparseness. The EM (1 square meter) and muon detectors (36 square meters) will be placed on a triangular grid of 15 meters side, to be compared with AGASA with 2.2 square meters detectors on a 1 km grid or AUGER with 10 square meters on a 1.5 km grid.

The shower axis can also be measured with fluorescence detectors. In this case, the shower appears as a sequential track propagating along a circle projected upon the celestial sphere. The signal is collected on a camera and the pixel "hit-pattern" defines the plane within which the shower axis lies, called Shower Detector Plane (SPD). The SPD is identified by the azimuthal and zenith angles of the unit vector $\vec{n}$ perpendicular to the plane. This vector can be found minimising the quantity $\sum_i \vec{r_i} \cdot \vec{n}$, where r_i are the signal-weighted normal vectors of fired pixels. The subsequent steps are to include the time–angle correlation information and minimise the expression

$$t_i = t_0 + \frac{R_{\mathrm{p}}}{c} \tan\left(\frac{\chi_0 - \chi_i}{2}\right) , \tag{63}$$

where t_0 is the time at which the shower axis vector passes by the closest point to the telescope at a distance R_{p}, c is the speed of light and t_i is the arrival time of the photons at camera pixel i, which is, in general, a signal-weighted average arrival time taken from the time sequence observed in a pixel, χ_0 is the angle of incidence of the shower axis within the SDP, and χ_i is the viewing angle of pixel i within the SDP as defined in Fig. 24 (right).

The parameters R_{p}, t_0 and χ_0 are extracted with a χ-square minimisation of the Eq. (63) comparing the t_i–χ_i correlation to the observed one for triggered pixels. Together with the SDP derived previously, the shower geometry is then fully determined and can also be expressed in terms of shower impact point, arrival direction, and ground impact time.

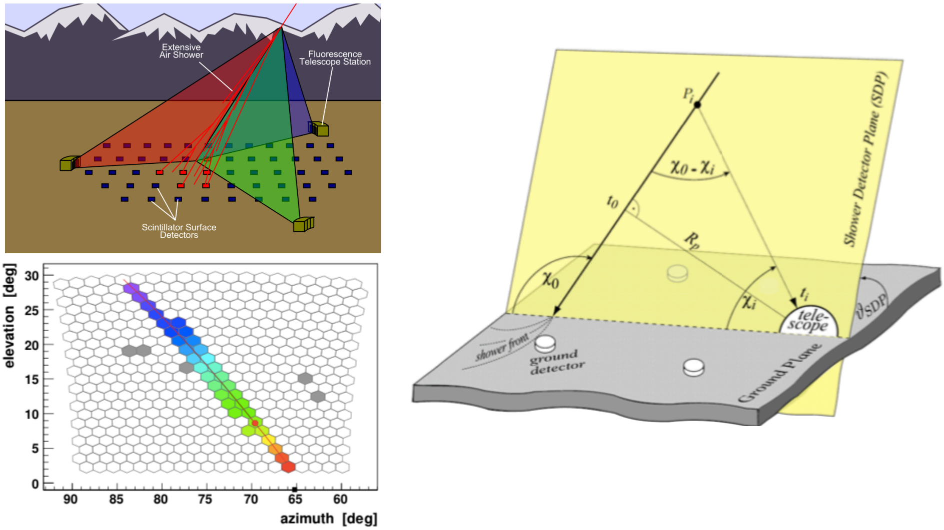

Fig. 24. (Colour on-line) Left bottom: The bottom figure shows the shower track (hit pattern) on the camera of a fluorescence detector. The colour of the pixels is the scale of the arrival time of the photons in each pixel. Left top: The stereo reconstruction of a shower with three fluorescence detectors. Right: The Shower Detector Plane (SPD) definition together with the parametrisation used.

The shower parameters reconstruction can be improved by combining information from different detectors, for example, the fluorescence detector and the ground array, more than one fluorescence detector, or both ground array coupled with more fluorescence detectors. This is particularly useful for the energy reconstruction.

Shower energy reconstruction

In IACT, the energy is directly derived from the photon density, therefore assuming a perfect calibration of the detectors, an absolute energy calibration is possible. In truth, the experimental effect and statistical fluctuation are present also in EM showers, limiting the energy resolution around 10–15%. For EAS array, instead, the energy is reconstructed using a different estimator and different methods according to the type of detectors used and their sparseness. As a matter of fact, the shower-by-shower fluctuations are more difficult to reconcile with Monte Carlo not only because of the well not modelled hadronic interactions, but also because the initial-particle type is unknown, the shower age can be different when it reaches the detectors, the shower components are detected with different efficiencies, threshold, *etc.*

The energy, therefore, cannot be reconstructed event-by-event with a good resolution. What is usually done is to build global variables as the global CRs flux, and then identify some class of events for which a better determination of the energy is possible and then set the energy scale for the given quantity used for its reconstruction. The estimator of the energy, the scale, resolution and bias are strictly dependent on the detectors type, their size, their sparseness.

For example, HAWC uses for the energy reconstruction of the shower a modified version of NKG in Eq. (47), adding a Gaussian term [60]. To estimate the primary cosmic ray energy, the lateral distribution of the measured signal as a function of the primary particle energy is used. Using the Monte Carlo simulation of proton-initiated shower, there is built a four-dimensional probability in bins of zenith angle, primary energy, PMT distance from the core in the shower plane and measured PMT signal amplitude. The resulting performance is evaluated via the bias distribution, defined as $\Delta_{\text{bias}} = \log(E_{\text{reco}}) - \log(E)$, *i.e.* the difference between the logarithms of the reconstructed and true energy values, shown in Fig. 25 (left). It is important to note that the reconstructed energy has a bias, *i.e.* is not well reconstructed, as seen in Fig. 25 (left). In this case, the reconstructed energy is smaller than the real (MC) energy. This is expected as, in this case, some of the particles in the shower are undetected and can be estimated only indirectly. This is not a problem in general, if the bias is constant but in this case, the bias depends on the energy and has to be taken into account, for example, for the reconstruction of the spectrum.

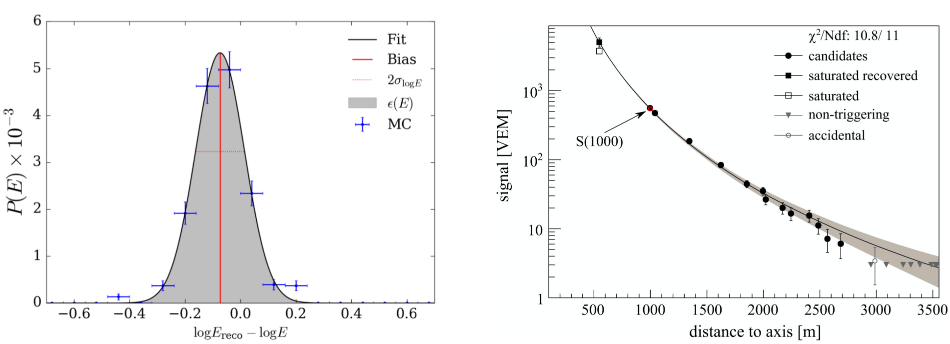

Fig. 25. Left: The bias estimator used by HAWC to evaluate the energy resolution σ and the bias, clearly indicated in the picture. Right: The shower size parameter $S(1000)$ used in AUGER for the energy assignment. The signal scale is in Vertical Equivalent Muons (VEM), which represent the charge produced by a vertical muon traversing an SD tank.

The Pierre Auger Collaboration (AUGER), instead, use a modified NKG

$$S(r) = S(r_{\text{opt}}) \left(\frac{r}{r_{\text{opt}}}\right)^{\beta} \left(\frac{r + r_1}{r_{\text{opt}} + r_1}\right)^{(\beta+\gamma)}, \tag{64}$$

where $r_1 = 700$ m and $S(r_{\rm opt})$ is the estimator of shower size used in the energy assignment. For the Surface Detector (SD), which is spaced by 1.5 km, the $r_{\rm opt} = 1000$ and then the shower size, a proxy of the shower energy, is $S(1000)$, shown in Fig. 25 (right). The choice of $r_{\rm opt} = 1000$ has been done showing by simulation that it is the one which is less shower-model dependant giving the most stable shower size reconstruction.

The $S(1000)$ has a zenith dependence due to the increasing atmospheric depth crossed by inclined showers, which is the cause of an attenuation of the EAS. To correct such an effect, it is used the Constant Intensity Cut (CIC) method [61], which is based on the assumption of isotropy of the cosmic ray flux. Isotropy implies that the arrival frequency of cosmic rays depends only on the primary energy and not on the arrival direction. In this way, the intensity of cosmic rays provides a common energy scale which can be used to extract the attenuation length of the EAS in the atmosphere that, in turn, can be used to take into account the atmospheric effects. For AUGER the shower size is parametrised as a third-degree polynomial in the form of $S(1000) = S_{38^\circ}(1 + ax + bx^2 + cx^3)$, where the $x = \cos^2(\vartheta) - \cos^2(38^\circ)$ and S_{38° is the zenith-angle-independent energy estimator and can be thought of as the signal $S(1000)$ that shower would have produced at a zenith angle 38°. To set the energy scale, it is better to use a calorimetric measurement as the one of the Fluorescence Detector (FD). Using "hybrid" events, *i.e.* event simultaneously recorded by SD and FD, it is possible to evaluate the energy scale as shown in Fig. 26 (for more detail, see [62]).

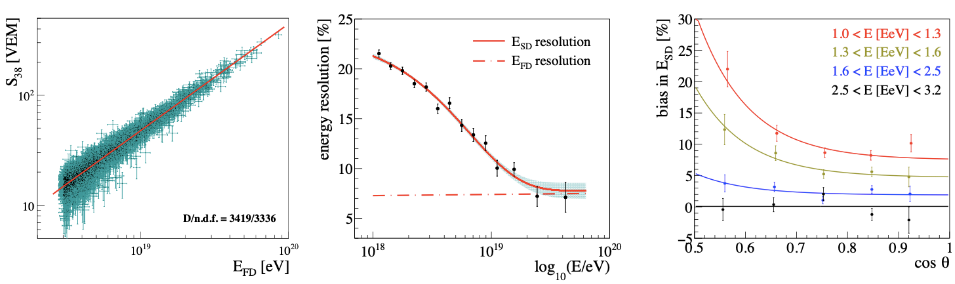

Fig. 26. Left: Correlation between the FD energies and S_{38°. Each event is shown with a point together with its individual uncertainties. The line is the best fit calibration curve. Energy resolution (center) and bias (right) for SD events estimated from "hybrid events" data [62].

Another interesting way of calibrating EAS arrays is to use the so-called Moon shadow, which is the hampering of cosmic rays by the Moon [60, 63]. The Moon–Earth system works as a spectrometer in which particle are deflected according to their rigidity. This causes an apparent shift of the Moon shadows of the cosmic rays, which changes according to their energy. The amount of such a displacement in the West–East direction can be approximated as 1.6°E [TeV]/Z. This shift is of the order of one degree for 1 TeV proton and it turns to be less than 0.1° for cosmic rays energy higher than 10 TeV. This technique allows to determine an absolute energy scale at TeV range but can also measure the point spread function of the detector or to estimate the antiproton–proton ratio at TeV energies.

3.2.5. The Large High-Altitude Array Shower Observatory

The Large High-Altitude Air Shower Observatory (LHAASO) project is a new generation all-sky EAS array strategically built to investigate the "cosmic ray connection" through a combined study of cosmic rays and γ-rays over several energy decades from 10^{11} to 10^{17} eV.

LHAASO will enable studies in cosmic ray physics and γ-ray astronomy that are currently unattainable by the existing instruments, given its duty cycle of 100% and the capability of surveying about 1/7 of the sky in any moment and cover 60% of the sky every day. The sensitivity achievable by LHAASO has been studied with Monte Carlo and it is compared to existing experiments in Fig. 27.

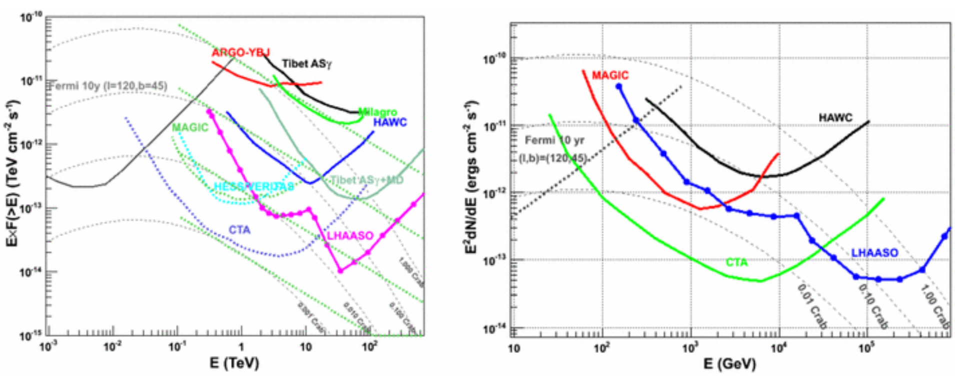

Fig. 27. The LHAASO sensitivity integral (left) and differential (right) compared with other experiments.

The LHAASO observatory is located at Mt Haizi (29°21'31"N, 100°08'15"E), few kilometres away from the city of Daocheng, in the Sichuan region, at an altitude of 4410 m a.s.l. (600 g/cm^2).

The LHAASO array (Fig. 28) is composed of many different types of detectors to be able to measure all shower components (EM, charged particles, muons) with a high efficiency and precision, but also on a wide area and with a low sparseness (see Fig. 29).

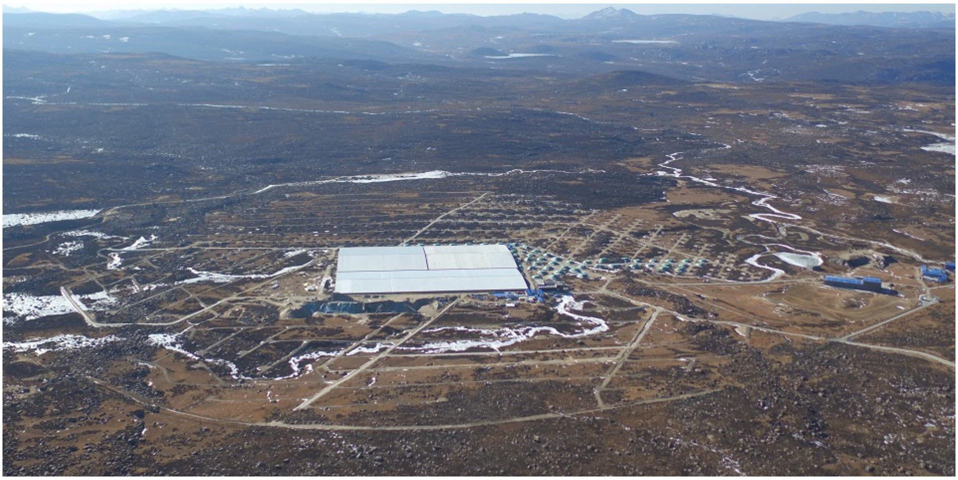

Fig. 28. A bird-view of the LHAASO observatory taken by a drone in March 2019. The 3 ponds are clearly visible together with the first EM and muon detectors.

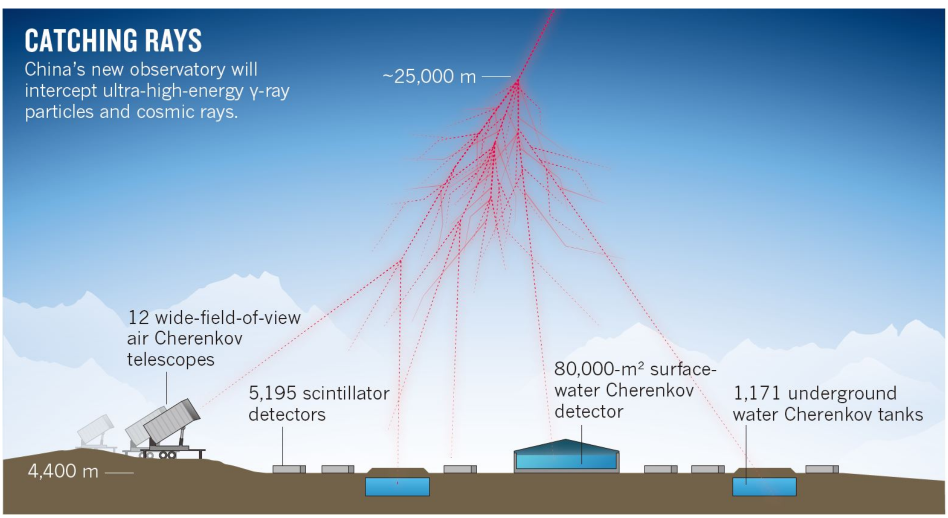

Fig. 29. A schematic illustration of the different detectors used in LHAASO for the detection of air shower [64].

The design concepts

The LHAASO schematic layout [65] is shown in Fig. 30 and consists of an array of EM and muon detectors distributed over a circular area of about 1.3 km^2 (KM2A). In its center, there is located a large Water Cherenkov Detector Array (WCDA) completed with an array of twenty Wide Field-of-View imaging telescopes working both with the Cherenkov and fluorescence light (WFCTA).

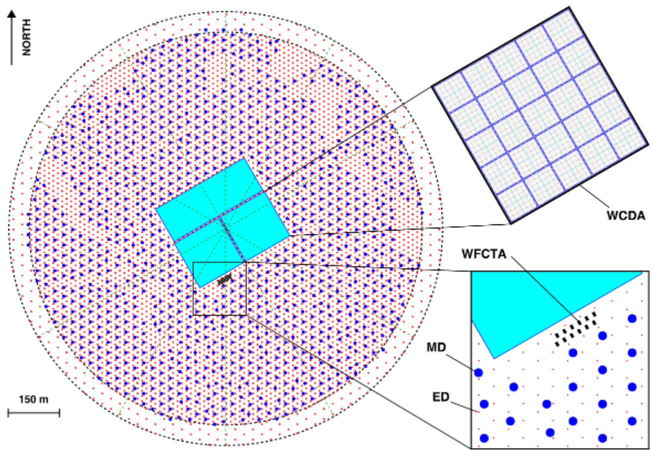

Fig. 30. (Colour on-line) Layout of LHAASO detectors. The big squares in the middle are the three ponds composing a square with a side of 300 meters. For one of the ponds also the cells composition is shown. The small/red dots show the position of the EM detectors, while the big/blue ones the position of muon detectors. The WFCTA telescopes are the small twelve squares in the zoom near the ponds. In the current design, the telescopes will be twenty.

The Water Cherenkov Detector Array (WCDA)

WCDA focuses on surveying the northern sky for steady and transient sources from 50 GeV to 20 TeV, with a very high background rejection power and a good angular resolution. It consists of three water ponds covering a total surface of 78,000 m^2 (more than 3 times the area instrumented by HAWC (https://www.hawc-observatory.org)) and a water depth of 4.4 meters, in which the charged secondary particles of the shower produce the Cherenkov light. The ponds are segmented in 5 m $\times$ 5 m cells by means of black plastic curtains to prevent the leakage of light among adjacent cells as shown in Fig. 31. Each cell is equipped with two Photomultipliers Tubes (PMT)

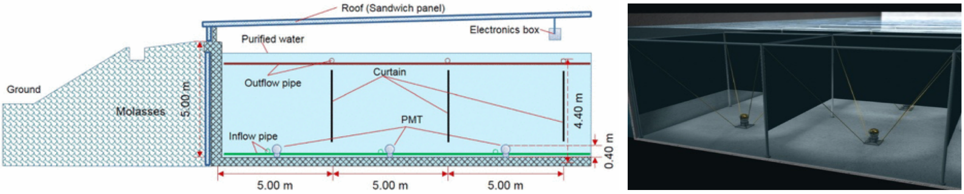

Fig. 31. WCDA design (left) and 3D model of a cell (right).

placed at the bottom of the water pointing upward. The original design intended to use an 8” PMT in the middle of the cell and a 1.5” PMT nearby to collect the light from upward. The use of two PMTs is meant to cover the large dynamic range keeping a good sensitivity for low number of photons. The bigger PMT covers the low light level and becomes then saturated for high number of photons, where, instead, the smaller one is working in its optimal range. By merging the information from the two PMTs, it is possible to correctly reconstruct the cell signal in the whole dynamic range, as shown in Fig. 32. Recently, it has been decided to replace, in the pond 2 and 3, the 8" PMT with a 20" PMT developed for the JUNO experiment [66] in order to improve the sensitivity at low energies. To cope with dynamic range also the 1.5" PMT will be replaced by a 3" PMT. This new configuration will lower the threshold from several hundred of GeV to 50 GeV and increase the effective area at 50 GeV by almost a factor of eight. For example, for a source with an energy spectrum index $\gamma = -2.62$ or -3.62, the integral significance can be increased by a factor of 1.5 or 3 [67]. With the use of larger PMTs, the effective area of the WCDA is around 10,000 square meters at 100 GeV, allowing to overlap with the FERMI-LAT energy range.

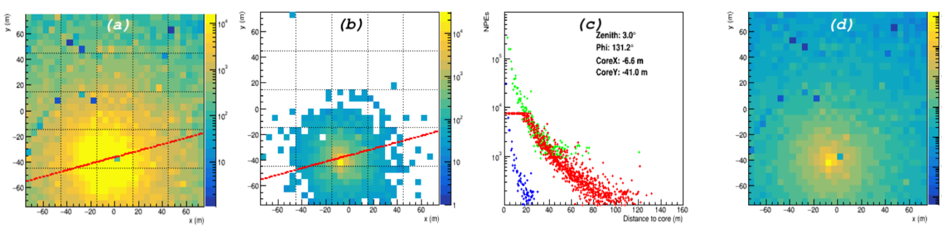

Fig. 32. (Colour on-line) A shower detected in WCDA. Here, there are shown signals from larger PMTs (a), from smaller ones (b) and combined (d). The lateral profile (c) is also shown. The black/blue colour represents small-PMT signals, the grey/red big-PMT signals. The light grey/green shows the overlapping of the blue one once rescaled to correctly overlap with the grey/red points.

The angular resolution is crucial for gamma-ray astronomy, where the source position can be reconstructed. As expected for any EAS array, also for LHAASO the angular resolution improves with the energy and becomes less than 0.1° above 10 TeV. The performance simulation study in Fig. 33 has been also recently validated on the first real data. To improve the reliability of the study, the so-called even–odd method has been used [68] , in which even cells and the odd ones are regarded as two independent detectors.

WCDA has the capability of doing gamma/hadron separation using the muon content of the shower. As a matter of fact, muons have large lateral momentum and then are easily identified as a large energy deposit away from the shower core (Fig. 34). This is done using a parameter called compactness which is defined as the ratio between the PMT multiplicity and the number of PE of the brightest PMT at a distance greater than 45 m from the core [69]. The parameter is quite effective in suppressing hadrons (0.27%

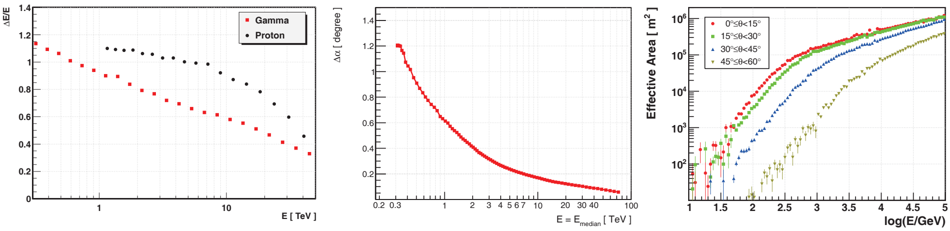

Fig. 33. LHAASO WCDA performances evaluated by simulation. The energy resolution on the left, the angular resolution in the middle and the effective area on the right.

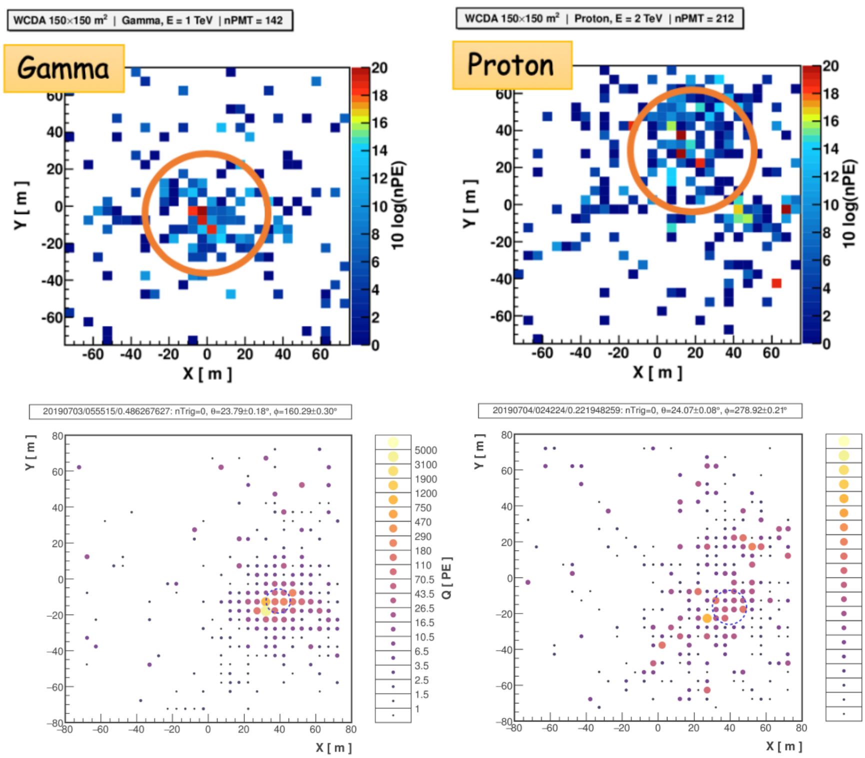

Fig. 34. Events as seen by the LHAASO WCDA. In the top row, MC event for a gamma (left) and a proton (right). In the bottom row, real events detected by WCDA-1: a gamma (left) and a proton (right).

survives) while keeping a reasonable gamma-ray efficiency (40%). Clearly, Multivariate analysis based on different approaches (K-Nearest Neighbour (K-NN) Classifier, H-matrix discriminant, Article Neural Network (ANN), Boosted Decision Trees with a Gradient boosting algorithm (BDTG), Support Vector Machine (SVM) have proven to achieve much better performance with respect to the simple compactness criteria [70].

The Kilometer-Square Array (KM2A)

The Kilometer-Square Array (KM2A) has been designed for studying cosmic-ray and gamma-ray sources at energies above 30 TeV in the northern sky and for measuring primary cosmic rays in the energy range from 10 TeV to 100 PeV. This detectors target the detection of γ-ray sources with a sensitivity of about 1% Crab Unit at 100 TeV as shown in Fig. 27.

It covers an area of about 1.2 km^2 and is composed of two types of detectors: electromagnetic particle detectors (ED) and muon detectors (MD). Each ED is composed of a 1 m^2 plane of scintillators covered by a 0.5 cm thick lead plate to increase its sensitivity by exploiting the pair-production of secondary photons, in order to improve the angular resolution and to lower the energy threshold (see Fig. 35). The KM2A-ED array is composed of 4931 EDs deployed on a triangular grid with a spacing of 15 m to instrument a circular area with a radius of 575 m. This central part is surrounded by an outer guard-ring instrumented with 311 EDs (30 m spacing) up to a radius of 635 m, mainly to improve the identification and the reconstruction of showers whose core is outside the instrumented area.

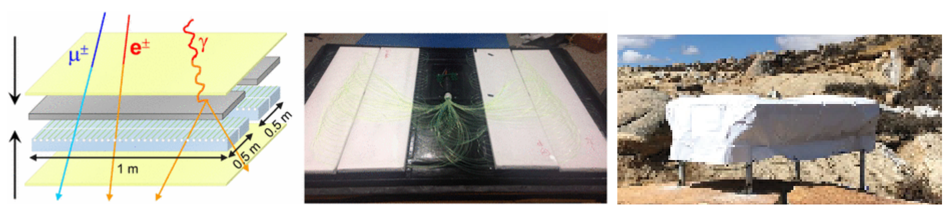

Fig. 35. The EM detectors characteristics (left). A module during construction (centre) and once installed on side (right).

The KM2A-MD array of muon detectors is composed of 1146 water Cherenkov tanks deployed on a triangular grid with a spacing of 30 m achieving a total sensitive area of 42,000 m^2. The tanks are buried under 2.5 m of soil (see Fig. 36), corresponding to 12 radiation lengths, both to reduce the punch-through due to the shower of electromagnetic particles and achieve a muon energy threshold of 1.3 GeV. The KM2A-MD will allow to reject cosmic nuclei background to a level of 10^{-4} at 50 TeV.

The large area covered by MD array will allow to reject hadronic shower background at a level of 10^{-4} at 50 TeV and even 10^{-5} at higher energies, hence producing a background-free samples of gamma-ray events at energies above 100 TeV. The highest sensitivity of KM2A is $\sim 1\%$ of the Crab Nebula flux in the energy range of 50 to 100 TeV for 1 yr. of observation [71]. At 30 TeV, the effective area of KM2A can reach about 0.8 km^2, the angular resolution is about 0.5°, and the energy resolution is about 27% for gamma

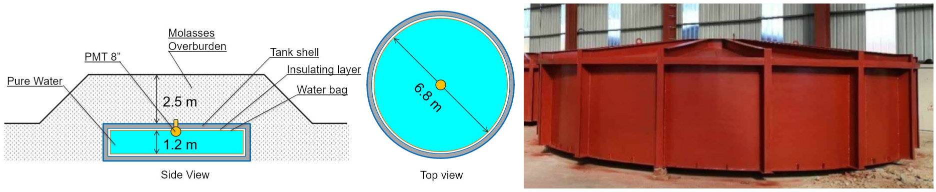

Fig. 36. The muon detectors characteristics (left). A picture of a tank before installation (right).

ray and 33% for proton. At 100 TeV, the corresponding values are 0.9 km^2, 0.3°, 20% and 25%.

The Wide Field-of-View Cherenkov Telescope Array (WFCTA)

WFCTA is composed of 20 wide field-of-view Cherenkov telescopes, each equipped with a mirror of about 2.14×2.36 m^2 composed of hexagonal facets and, in its focal plane, a square camera of 32×32 pixels with a pixel angular size of 0.5° (25 mm linear size). With this configuration, a telescope will have a field of view of $14° \times 16°$.

To extend the spectrum to higher energies and make a connection with experiments, such as Telescope Array (TA) and Pierre Auger, the WFCTA telescopes will be re-arranged to measure the fluorescence light from showers and monitor from a distance of 4 or 5 km the space above the ground array. Sixteen telescopes of the main detector array will be moved far from LHAASO ("Tower FD" in Fig. 37 (right)) facing its core and will cover elevations from 3° to 59° and two more telescopes will cover elevations from 10° to 24°, thus observing showers from a direction perpendicular to the main array (see "Side FD" in Fig. 37 (right)). Two more telescopes will be in symmetrical position ("Side FD") with respect to the former two. Showers above 100 PeV will be detected in stereoscopic mode in order to achieve a

Fig. 37. The first six telescopes of WFCTA installed on-site (left). A picture of one of the 6 telescopes already installed on site (center), where the imaging camera is visible in front of the mirror (black box). The arrangement of the WFCTA for CRs composition studies (right). Telescopes are re-arranged in 3 regions, 4–5 km away from the core, to monitor the sky over WCDA.

resolution on the reconstruction of the shower maximum $X_{\rm max}$ as low as 25 g/cm^2. Muon content and $X_{\rm max}$ are used for composition measurement around the *knee* of the spectrum [72, 73].

The commissioning of the array is advancing quite well and within schedule. In Fig. 38 (left) the current situation is shown, with the pond WCDA-1 already operational while WCDA-2 is being filled with water. Many preliminary results have been presented recently at the ICRC conference (`https://pos.sissa.it/358/`). The first pool of WCDA was completed at the beginning of 2019 and, since then, the detector has been running in commissioning mode. Many improvements have been made both in detector simulation and reconstruction methods. Comparisons between data and MC samples [74] have shown a good agreement concerning fundamental quantities, such as lateral distribution, or core and angular resolution of shower, and also the trigger rate measured agrees within 8% with MC prediction. The first two WFCTA telescopes are commissioned and successfully operated, demonstrating also their ability to work with moon-light. In Fig. 38 (right), an event simultaneously detected by two telescopes and the WCDA-1 is shown. In particular, there has been shown [75] a preliminary energy calibration using Moon shadow [63, 76]. Sensitivity to this shadow

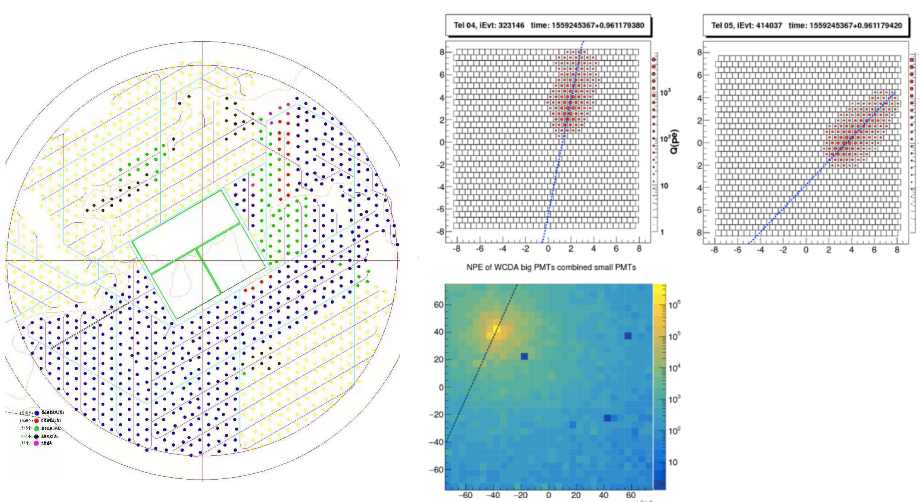

Fig. 38. (Colour on-line) Status of the LHAASO commissioning. Left: The WCDA-1 is fully operational. WCDA-2 is being filled with water and should be operational by beginning of 2020. In WCDA-3 the installation of the system is on-going. The KM2A detectors already installed and under commissioning are the one marked in blue, while the ones already operational are marked in green and red. Right: A cosmic-ray shower simultaneously detected by two telescopes (top row) and the WCDA-1 (bottom).

proves an angular resolution at least as good as the dimension of the shadow which is $< 0.5°$. The size and displacement of the shadow can be correlated with CRs energy via MC simulation.

Figure 39 shows the Moon shadow as measured by the WCDA for different ranges of the energy proxy n_{Fit}, which is the number of fired cells. The corresponding energy is not yet reported as the study of the systematics is still on-going.

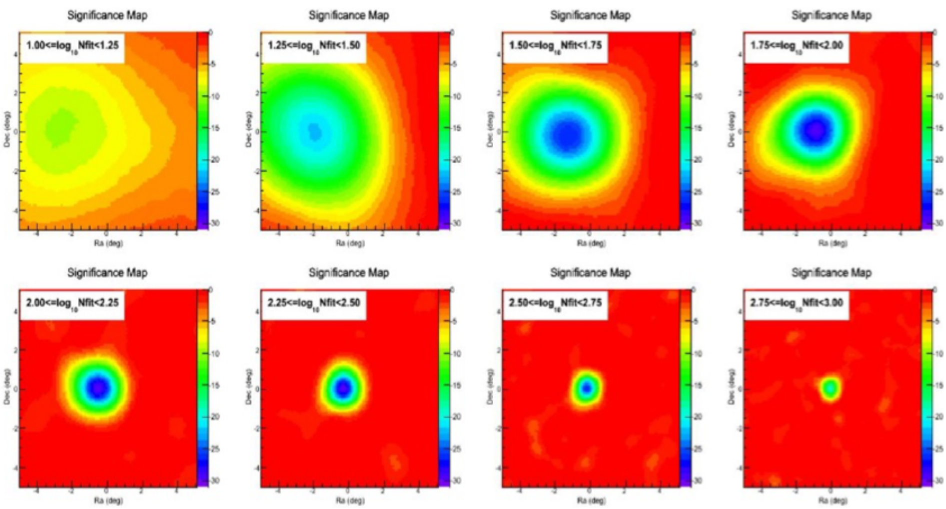

Fig. 39. The significance of the Moon shadow reconstructed by WCDA for different values of the energy proxy n_{Fit}. The shift from the (0,0) is evident at lower energies (top-left) and tend to disappear at higher energies (bottom-right).

LHAASO will be completed by the end of 2020 and start science operation in 2021. In 2020, a quarter of the array will be put in science mode to allow to calibrate the energy scale and do some preliminary studies. As a matter of fact, only the WDCA-1 has the same area as HAWC, but with a complete coverage and more sensitivity. So including also the EDs an MDs already operational, this quarter of the full array has already the capability of improving present HAWC results and allow to perfectly characterise the detectors, the reconstruction techniques, the analysis pipeline, to be ready to go in science mode with the full array as soon as it will be commissioned.

REFERENCES

[1] R.L. Diehl, *Eur. Phys. J. D* **55**, 509 (2009).

[2] P. Blasi, *Astron. Astrophys. Rev.* **21**, 70 (2013).

[3] M. Ostrowski, *Astropart. Phys.* **18**, 229 (2002).

[4] A.M. Hillas, *Annu. Rev. Astron. Astrophys.* **22**, 425 (1984).

[5] P.O. Lagage, C.J. Cesarsky, *Astron. Astrophys.* **118**, 223 (1983).

[6] A.M. Hillas, *J. Phys. G* **31**, R95 (2005).

[7] J.R. Hörandel, *Astropart. Phys.* **21**, 241 (2004).

[8] J.R. Hörandel, *Astropart. Phys.* **19**, 193 (2003).

[9] V. Ptuskin, V. Zirakashvili, E.-S. Seo, *Astrophys. J.* **718**, 31 (2010).

[10] M. Cardillo, M. Tavani, A. Giuliani, *Nucl. Phys. B — Proc. Suppl.* **256**–**257**, 85 (2014).

[11] K. Greisen, *Phys. Rev. Lett.* **16**, 748 (1966).

[12] G.T. Zatsepin, V.A. Kuz'min, *ZhETF Pisma Redaktsiiu* **4**, 114 (1966).

[13] W.R. Leo, *Techniques for Nuclear and Particle Physics Experiments: A How-to Approach*, Springer-Verlag, 1987, DOI:10.1007/978-3-642-57920-2.

[14] T. Ferbel, *Experimental Techniques in High Energy Physics*, 1st ed., in: *Frontiers in Physics*, Menlo Park, CA: Addison-Wesley, 1987, contains articles by K. Kleinknecht, F. Sauli, G. Charpak, C. Fabjan, U. Amaldi, *etc.*, `https://cds.cern.ch/record/110951`

[15] G.F. Knoll, *Radiation Detection and Measurement*, 4th ed., New York, NY: Wiley, 2010, `https://cds.cern.ch/record/1300754`

[16] C. Leroy, P.-G. Rancoita, *Principles of Radiation Interaction in Matter and Detection*, 4th ed., World Scientific, 2016, DOI:10.1142/9167.

[17] K. Kleinknecht, *Detectors for Particle Radiation*, Cambridge Univ. Press, 1986, `https://cds.cern.ch/record/108093`

[18] C. Grupen, A. Böhrer, L. Smolik, *Particle Detectors*, Cambridge Univ. Press, 1996, `https://cds.cern.ch/record/306826`

[19] R.K. Bock, A. Vasilescu, *The Particle Detector Briefbook. Accelerator Physics*, Berlin: Springer, 1998, DOI:10.1007/978-3-662-03727-0.

[20] Cross Sections — High Energy Physics Made Painless, `https://ed.fnal.gov/painless/pdfs/cross.pdf`

[21] H. Bethe, *Ann. Phys.* **39**, 325 (1930).

[22] H. Bethe, W. Heitler, *Proc. R. Soc. London, Ser. A* **146**, 83 (1934).

[23] M. Tanabashi *et al.*, *Phys. Rev. D* **98**, 030001 (2018).

[24] C.F. Powell, P.H. Fowler, D.H. Perkins, *The Study of Elementary Particles by the Photographic Method: An Account of the Principal Techniques Discoveries Illustrated by an Atlas of Photomicrographs*, London: Pergamon, 1959, `https://cds.cern.ch/record/107069`

[25] M.E. Peskin, D.V. Schroeder, E. Martinec, *Phys. Today* **49**, 69 (1996).

[26] M.J. Berger, S.M. Seltzer, *Tables of Energy Losses and Ranges of Electrons and Positrons*, NASA Special Publication, vol. 3012.

[27] U. Amaldi, *Phys. Scr.* **23**, 409 (1981).

[28] O. Dovzhenko, A. Pomanskii, *JETP* **18**, 187 (1964) http://www.jetp.ac.ru/cgi-bin/dn/e_018_01_0187.pdf

[29] B. Rossi, *High-energy Particles*, Englewood Cliffs, N.J.: Prentice-Hall, 1965.

[30] E. Longo, I. Sestili, *Nucl. Instrum. Methods* **128**, 283 (1975) [*Erratum ibid.* **135**, 587 (1976)].

[31] E. Longo, L. Luminari, *Nucl. Instrum. Methods Phys. Res. A* **239**, 506 (1985).

[32] D. Acosta *et al.*, *Nucl. Instrum. Methods Phys. Res. A* **316**, 184 (1992).

[33] N. Akchurin *et al.*, *Nucl. Instrum. Methods Phys. Res. A* **399**, 202 (1997).

[34] C. Fabjan, *Nucl. Instrum. Methods Phys. Res. A* **252**, 145 (1986).

[35] D.T. Haar (Ed.), *75 — The Limits of Applicability of the Theory of Bremsstrahlung by Electrons and of the Creation of Pairs at Large Energies*, in: *Collected Papers of L.D. Landau*, Pergamon, 1965, pp. 586–588, DOI:10.1016/B978-0-08-010586-4.50080-8.

[36] A.B. Migdal, *Phys. Rev.* **103**, 1811 (1956).

[37] S. Klein, *Rev. Mod. Phys.* **71**, 1501 (1999).

[38] P.K. Grieder, *Extensive Air Showers: High Energy Phenomena and Astrophysical Aspects — A Tutorial, Reference Manual and Data Book*, Berlin, Heidelberg: Springer, 2010, DOI:10.1007/978-3-540-76941-5.

[39] P.L. Anthony *et al.*, *Phys. Rev. D* **56**, 1373 (1997) [arXiv:hep-ex/9703016].

[40] J. Matthews, *Astropart. Phys.* **22**, 387 (2005).

[41] M. Glasmacher *et al.*, *Astropart. Phys.* **12**, 1 (1999).

[42] R. Engel, *Air Shower Calculations with the New Version of SIBYLL*, 26$^{\text{th}}$ International Cosmic Ray Conference (ICRC26), vol. 1, 1999, p. 415.

[43] J. Engel, T.K. Gaisser, P. Lipari, T. Stanev, *Phys. Rev. D* **46**, 5013 (1992).

[44] T. Pierog, R. Engel, D. Heck, G. Poghosyan, *EPJ Web Conf.* **89**, 01003 (2015).

[45] W. Galbraith, J.V. Jelley, *Nature* **171**, 349 (1953).

[46] B. Acharya *et al.*, *Astropart. Phys.* **43**, 3 (2013).

[47] V. Vassiliev, P.F. Brousseau, S.J. Fegan, *Astropart. Phys.* **28**, 10 (2007) [arXiv:astro-ph/0612718].

[48] B.S. Acharya *et al.* [Cherenkov Telescope Array Consortium], *Science with the Cherenkov Telescope Array*, 2019, DOI:10.1142/10986.

[49] R.M. Baltrusaitis *et al.*, *Nucl. Instrum. Methods Phys. Res. A* **240**, 410 (1985).

[50] H. Kawai *et al.*, *Nucl. Phys. B — Proc. Suppl.* **175–176**, 221 (2008).

[51] J. Abraham *et al.*, *Nucl. Instrum. Methods Phys. Res. A* **620**, 227 (2010).

[52] L. Anchordoqui *et al.*, *Ann. Phys.* **314**, 145 (2004).

[53] K. Kamata, J. Nishimura, *Prog. Theor. Phys. Suppl.* **6**, 93 (1958).

[54] K. Greisen, *Annu. Rev. Nucl. Part. Sci.* **10**, 63 (1960).

[55] M. Nagano *et al.*, *J. Phys. Soc. Jpn.* **53**, 1667 (1984).

[56] A.M. Hillas, J.D. Hollows, H.W. Hunter, D.J. Marsden, *Calculations on the Particle and Energy-loss Densities in Extensive Air Showers at Large Axial Distances*, International Cosmic Ray Conference, vol. 29, 1970, p. 533.

[57] G.B. Khristiansen *et al.*, *Study of EAS Muon Component*, International Cosmic Ray Conference, vol. 8, 1977, p. 148.

[58] T.K. Gaisser, A.M. Hillas, *Reliability of the Method of Constant Intensity Cuts for Reconstructing the Average Development of Vertical Showers*, International Cosmic Ray Conference, vol. 8, 1977, p. 353.

[59] J. Linsley, A.A. Watson, *Phys. Rev. Lett.* **46**, 459 (1981).

[60] R. Alfaro *et al.*, *Phys. Rev. D* **96**, 122001 (2017) [`arXiv:1710.00890 [astro-ph.HE]`].

[61] J.C. Arteaga-Velázquez *et al.*, *Nucl. Phys. B — Proc. Suppl.* **196**, 183 (2009).

[62] V. Verzi, *Measurement of the Energy Spectrum of Ultra-high Energy Cosmic Rays Using the Pierre Auger Observatory*, $36^{\rm th}$ International Cosmic Ray Conference (ICRC2019), vol. 36, 2019, p. 450.

[63] B. Bartoli *et al.*, *Astropart. Phys.* **90**, 20 (2017).

[64] D. Cyranoski, *China's Mountain Observatory Begins Hunt for Origins of Cosmic Rays*, DOI:10.1038/d41586-019-01467-1.

[65] X. Bai *et al.*, The Large High Altitude Air Shower Observatory (LHAASO) Science White Paper, `arXiv:1905.02773 [astro-ph.HE]`.

[66] N. Anfimov, *JINST* **12**, C06017 (2017), `http://stacks.iop.org/1748-0221/12/i=06/a=C06017`

[67] C. Mingjun, *New 20" PMT for LHAASO*, $9^{\rm th}$ Workshop on Air Shower Detection at High Altitudes, 2018, `http://wasdha2018.inr.ac.ru/programme/talks/Chen_Mingjun.pdf`

[68] H. Li, *Comparison of Measured and Simulated Data with LHAASO-WCDA Run Data*, $36^{\rm th}$ International Cosmic Ray Conference (ICRC2019), vol. 36, 2019, p. 333.

[69] Y. Guo, X. Chang, H. Hu, Z. Yao, *The Significance of the Water Cherenkov Detector Array (WCDA) to Multi-TeV Gamma Rays Sources*, $36^{\rm th}$ International Cosmic Ray Conference (ICRC2019), vol. 36, 2019, p. 277.

[70] X. Wang, *Gamma Hadron Separation Using Traditional Single Parameter Method and Multivariate Algorithms with LHAASO-WCDA Experiment*, $36^{\rm th}$ International Cosmic Ray Conference (ICRC2019), vol. 36, 2019, p. 820.

[71] Y. Liu *et al.*, *Astrophys. J.* **826**, 63 (2016) [`arXiv:1605.05472 [astro-ph.HE]`].

[72] Z. Cao [LHAASO Collaboration], *Measurement of the Knees of Proton and H and He Spectra Below 1 PeV*, 15$^{\rm th}$ International Conference on Topics in Astroparticle and Underground Physics (TAUP 2017), Sudbury, Ontario, Canada, July 24–28, 2017, 2018, p. 5, http://indico.cern.ch/event/606690/contributions/2606196/

[73] Z. Cao [LHAASO Collaboration], *Frascati Phys. Ser.* **64**, 85 (2017).

[74] X. Li *et al.*, *Simulation and Real Data Analysis of the LHAASO-WCDA Dynamic Range Extension System*, 36$^{\rm th}$ International Cosmic Ray Conference (ICRC2019), vol. 36, 2019, p. 335, https://pos.sissa.it/358/335/

[75] Y. Wang, M.Z.Z.C.X. Zhang, *The Energy Calibration Using the Moon Shadow of LHAASO-WCDA Detector*, 36$^{\rm th}$ International Cosmic Ray Conference (ICRC2019), vol. 36, 2019, p. 463, https://pos.sissa.it/358/463/

[76] K. Kawata *et al.*, *Absolute Energy Scale Calibration of Multi-TeV Cosmic Rays Using the Moon's Shadow Observed by the Tibet Air Shower Array*, 29$^{\rm th}$ International Cosmic Ray Conference (ICRC29), vol. 6, 2005, p. 53, http://cds.cern.ch/record/964727